GLIAL ALTERATIONS FROM EARLY TO LATE STAGES IN A MODEL OF ALZHEIMER'S DISEASE : EVIDENCE OF AUTOPHAGY INVOLVEMENT IN Aβ INTERNALIZATION.

CARLOS POMILIO *(1) PATRICIO PAVIA *(1); ROXANA MAYRA GOROJOD (2) ANGELES VINUESA (1); AGUSTINA ALAIMO (2) VERONICA GALVAN (3); MONICA LIDIA KOTLER (2) JUAN BEAUQUIS (1); FLAVIA SARAVIA (1).

1-INSTITUTO DE BIOLOGIA Y MEDICINA EXPERIMENTAL CONICET
DEPARTAMENTO DE QUIMICA BIOLOGICA FACULTAD DE CIENCIAS EXACTAS Y NATURALES UNIVERSIDAD DE BUENOS AIRES.

2-IQUIBICEN-CONICET DEPARTAMENTO DE QUIMICA BIOLOGICA FACULTAD DE CIENCIAS EXACTAS Y NATURALES UNIVERSIDAD DE BUENOS AIRES.

3- DEPARTMENT OF PHYSIOLOGY AND THE BARSHOP INSTITUTE FOR LONGEVITY AND AGING STUDIES, UNIVERSITY OF TEXAS HEATH SCIENCE CENTER AT SAN ANTONIO, TEXAS, UNITED STATES OF AMERICA.

* EQUAL CONTRIBUTION

RUNNING TITLE: Neuroinflammation progress in a model of AD

Number of text pages 23
Number of Figures 8

CORRESPONDING AUTHOR: FLAVIA SARAVIA, INSTITUTO DE BIOLOGÍA Y MEDICINA EXPERIMENTAL CONICET AND DEPARTAMENTO DE QUÍMICA BIOLÓGICA, FACULTAD DE CIENCIAS EXACTAS Y NATURALES, UNIVERSIDAD DE BUENOS AIRES, OBLIGADO 2490 - 1428- BUENOS AIRES ARGENTINA PHONE. 54-11-4576-3300 EXT 423
fsaravia@qb.fcen.uba.ar and fesaravia@gmail.com

This work was supported by grants to JB from Alberto Roemmers Foundation and Agencia Nacional de Promoción de Ciencia y Tecnología of Argentina (ANPCyT) PICT 2013- #2645 and to FS from ANPCyT PICT 2011 #1012 2014#1168 and PIP CONICET PIP 2013-2015 Nº 473

KEY WORDS: Hilus, Stratum radiatum; Neuroinflammation; Astrocytes; Microglia; LC3; Ubiquitin; AD

ABSTRACT

Alzheimer's disease (AD) is a progressive neurodegenerative disease without effective therapy. Brain amyloid deposits are classical histopathological hallmarks that generate an inflammatory reaction affecting neuronal and glial function. The identification of early cell responses and of brain areas involved could help to design new successful treatments. Hence, we studied early alterations of hippocampal glia and their progression during the neuropathology in PDAPP-J20 transgenic mice, AD model, at 3, 9 and 15 months (m) of age. At 3 m, before deposits formation, microglial Iba1+ cells from transgenic mice already exhibited signs of activation and larger soma size in the hilus, alterations appearing later on stratum radiatum. Iba1 immunohistochemistry revealed increased cell density and immunoreactive area in PDAPP mice from 9 m onwards selectively in the hilus, in coincidence with prominent amyloid Congo red + deposition. At pre-plaque stages, GFAP+ astroglia showed density alterations while, at an advanced age, the presence of deposits was associated with important glial volume changes and apparently being intimately involved in amyloid degradation. Astrocytes around plaques were strongly labeled for LC3 until 15 m in Tg mice, suggestive of increased autophagic flux. Moreover, β-Amyloid fibrils internalization by astrocytes in *in vitro* conditions was dependent on autophagy. Co-localization of Iba1 with ubiquitin or p62 was exclusively found in microglia contacting deposits from 9 m onwards, suggesting torpid autophagy. Our work characterizes glial changes at early stages of the disease in PDAPP-J20 mice, focusing on the hilus as an especially susceptible hippocampal subfield, and provides evidence that glial autophagy could play a role in amyloid processing at advanced stages.

INTRODUCTION

Alzheimer's disease (AD) is a devastating progressive neurodegenerative disorder with no effective therapies available. In humans, AD is characterized by personality changes, increasing memory loss and cognitive impairment, being the first cause of dementia. The hippocampus is a central component in learning and memory processes being one of the main regions susceptible to stress and affected in AD (Marlatt and Lucassen, 2010; de Kloet et al., 1998).

Loss of hippocampal neurons, central inflammation, amyloid extracellular deposition and neurofibrillary tangles, are amongst the more important pathological hallmarks in the AD brain (Blennow et al., 2006; Dubois et al., 2010). Reactive astro- and microglial cells around senile plaques, mainly composed of Aβ peptides with a high proportion of Aβ1-42, constitute a frequent event in late stages of the disease found in brains from patients and rodents modelizing AD as well (Nagele et al., 2004; Rodriguez et al., 2009). Plaque load was historically considered for definitive post mortem diagnosis and a major therapeutic target in AD. However, the clinical relevance of amyloid deposits is at least controversial taking into account the poor correlation between the presence of plaques in the brain and the degree of cognitive impairment (Bansal et al., 2012).

As plaque deposition might be a late event in AD, there is a clear necessity to increase our knowledge about early pathological signs of the disease, including specific cell responses and areas primary involved, with the purpose of identifying novel targets and new effective biomarkers as well.

Recently, soluble Aβ peptides, before aggregation and deposition, were associated with impairments of neuronal functionality. Astroglia, controlling the volume and composition of the extracellular space, can sense toxic compounds, like amyloid peptides, to mount a rapid reaction. In line with this notion, our group reported a lower number of GFAP+ cells in addition to premature astrocytic changes in hippocampal CA1 region of PDAPP mice at 5 months of age, when no amyloid deposits were found but soluble APP derived peptides were quantifiable in brain homogenates (Beauquis et al., 2014; Beauquis et al., 2013). Morphological changes in GFAP+ cells might reflect glial dysfunction and consequently loss of support for neurons, as it was suggested by Steele et al (Steele and Robinson, 2012).

Microglial cells represent the brain immune system and actively survey the cerebral microenvironment with their motile processes. The phenotype of these cells can change according to the detection of environmental alterations, due, for instance, to tissue damage. As it was previously mentioned, activated microglia found around senile plaques is well documented (Mosher and Wyss-Coray, 2014; Verkhratsky et al., 2014b) but little is known about microglia reactivity in the hippocampus during the first stages of AD, before plaque deposition. Among the few studies exploring this aspect of AD pathogenesis, there is a report showing the presence of CD68+ microglia cells in the hippocampus of young hAPP-J20 (Wright et al., 2013), and an interesting *in vitro* study stating that primary murine microglia can react to Aβ1-42 fibrils but not to oligomers, the predominant species in early AD (Ferrera et al., 2014).

Multiple reports evidence the central implication of glia in Aβ peptide clearance. Mandrekar and coworkers demonstrated that microglia are able to internalize fluorescently labeled soluble Aβ in vitro through macropinocytosis, suggesting a crucial role of this cell type in the maintenance of Aβ homeostasis in the brain (Mandrekar et al., 2009). In addition, the authors confirm the uptake of fibrillar forms of Aβ by cultured microglia but involving a different cellular compartment than soluble forms.

The exposure of astrocytes to Aβ induces cellular activation evidenced by cell hypertrophy and processes extension. Although less efficiently than microglia, astrocytes appear to be able to internalize Aβ and are implicated in its clearance, possibly in a mechanism to reduce Aβ availability to neurons (Mandrekar et al., 2009; Mohamed and Posse, 2011; Pihlaja et al., 2008; Rodriguez et al., 2009). However, chronic exposure of astrocytes to Aβ might have detrimental consequences by inducing release of glial inflammatory cytokines and release of nitric oxide, which could lead to neuronal and glial cell death.

Even though glial cells have been shown to be able to take up Aβ, their capacity to degrade it is still unclear. Given its size and structure, aggregated Aß species could preferentially be cleared

from the cell trough the autophagic machinery (Dantuma and Bott, 2014). Autophagy is a prominent degradation pathway for organelles and aggregated proteins like APP-derived peptides. Autophagy is activated in AD brains (Yu et al., 2005) , apparently involved in Aβ clearance facilitation (Bjorkoy et al., 2005; Jaeger and Wyss-Coray, 2009; Ravikumar et al., 2004). Autophagosomes and other prelysosomal autophagic vacuoles were unequivocally identified in affected neurons from AD brains (Nixon et al., 2005). The inhibition of mTOR (a central negative regulator of autophagic activity) by rapamycin administration is associated with anti-aging effects (Harrison et al., 2009; Wilkinson et al., 2012; Santos et al., 2011). In PDAPP mice, rapamycin promotes autophagy, consequently reduces Aβ levels and abolishes cognitive deficits measured as performance in Water Morris maze both when administered before (Spilman et al., 2010) or after (Lin et al., 2013) the onset of AD-like cognitive deficits. Autophagy induction by rapamycin treatment is associated with increased levels of microtubule-associated protein-light-chain 3 (LC3) during autophagosome formation. LC3 can be shown as “labeled puncta” by immunohistochemistry and is located mostly in hippocampal neuronal processes (Spilman et al., 2010). Autophagy, in the CNS has been studied mainly in neurons, remaining largely unexplored in other cell types. At least to our knowledge, few studies investigated the involvement of autophagy in astro- and microglia in neurodegenerative diseases.

In this study we report glial changes in the hippocampus of PDAPP-J20 mice at different stages in the progression of amyloid pathology, as well as associated alterations in autophagy. We show that microglial morphology changes start before amyloid plaque deposition, suggesting an early response to disturbances in the hippocampal microenvironment, with particular emphasis in the hilus of the dentate gyrus. We further demonstrate the involvement of autophagy in glial cells associated to amyloid deposition. Additionally to our *in vivo* approach, *in vi*tro experiments allowed us to confirm that Aβ internalization depends on the autophagic process on astrocytes.

MATERIALS AND METHODS

Animals

The derivation and characterization of PDAPP-J20 [hAPP(J20)] mice has been described elsewhere (Hsia et al., 1999; Mucke et al., 2000; Selkoe, 2000; Galvan et al., 2006; Roberson et al., 2007; Beauquis et al., 2014). This strain, a recognized model of AD, carries the hAPP gene with the familial AD Swedish and Indiana mutations, develops amyloid pathology and behavioral alterations in a progressive fashion (Galvan et al., 2006), and also shows evidence of Tau hyper-phosphorylation (Simon et al., 2009). Transgenic mice were maintained by heterozygous crosses with C57BL/6J mice (Jackson Laboratories, Bar Harbor, ME) in our animal facility (Institute of Biology and Experimental Medicine, UBA–CONICET; NIH Assurance Certificate # A5072-01) and were housed under controlled conditions of temperature (22ºC) and humidity (50%) with 12 h/12 h light/dark cycles (lights on at 7:00 am). PDAPP-J20 mice were heterozygous with respect to the transgene, verified by PCR using specific primers. Non transgenic littermates were used as controls (Ntg group). All animal experiments followed the NIH Guide for the Care and Use of Laboratory Animals and were approved by the Ethical Committee of the Institute of Biology and Experimental Medicine. All efforts were done to reduce the number of mice used in the study as well as to minimize animal suffering and discomfort.

Tissue processing

Animals were anesthetized with ketamine (80 mg/kg BW, i.p.; Holliday-Scott, Argentina) and xylazine (10mg/kg BW, i.p.; Bayer, Argentina) and then transcardially perfused with 30 mL of 0.9% saline followed by 30 mL of 4% paraformaldehyde in 0.1M phosphate buffer, pH 7.4. Brains were removed from the skull, dissected, fixed overnight in the 4% paraformaldehyde solution at 4ºC and then cut coronally at 60 µm in a vibrating microtome (Vibratome 1000P). Sections were stored in a cryoprotectant solution (25% glycerol, 25% ethylene glycol, 50% phosphate buffer 0.1 M, pH 7.4) at -20ºC until use. All immunohistochemical techniques and Congo red staining were performed on free-floating sections. For plaque load, cell number and morphometric analyses, six brain sections per mouse and five mice per experimental group were evaluated. In all detailed cases in the following sections, ventral and dorsal hippocampi were considered for plaque load, volume, cell counting, and optical density determinations. The investigator was blinded to the corresponding genotype in every case.

Congo red staining and amyloid plaque load

Hippocampal amyloid plaque load was assessed in CA1 stratum radiatum and hilus from brain sections stained with Congo red (Wilcock et al., 2006). Briefly, coronal brain sections were incubated for 5 min at room temperature (RT) in a solution containing 0.2% Congo red (Biopack, Argentina), 3% NaCl (to saturation) and 0.01% sodium hydroxide in 80% ethanol. After rinsing, sections were put on gelatin-coated slides, air-dried overnight, dehydrated using ethanol and cleared in xylene. Slides were coverslipped using Canada balsam (Biopack, Argentina). Images from Congo red-stained sections were obtained under a 40X magnification in a Nikon Eclipse E200 microscope. Plaque load was determined as the percentage of the reference area that was occupied by Congo red-stained amyloid plaques. The reference area was measured by manually tracing strata radiatum and the hilus using ImageJ software NIH, (Abramoff et al., 2004) With the same software we determined Congo red stained area using an operator-determined gray value threshold.

Immunohistochemistry and immunofluorescence

Iba1 immunohistochemistry counterstained with Congo red was done to measure the morphological, numerical and distribution characteristics of microglia and their spatial relationship with amyloid plaques. Iba1/Ubiquitin double-immunofluorescence was done to evaluate protein

deposition inside microglial cells associated or not associated to amyloid plaques. GFAP/LC3 double-immunofluorescence was carried out in order to evaluate alterations in astrocyte autophagy in relation to their distance to the amyloid plaques.

Nonspecific antigenic sites were blocked by a solution of PBS containing 0.1% Triton X-100 and 10% normal goat serum. Then, sections were incubated overnight (2 overnights for Iba1) at 4ºC with the following primary antibodies: mouse monoclonal anti-GFAP (1:400, G-3893, Sigma), mouse monoclonal anti-Ubiquitin (1:1000, MAB1510, Chemicon, USA), rabbit polyclonal anti-Iba1 (1:1500, Wako Pure Chemical Industries, Osaka, Japan) and rabbit polyclonal anti-LC3 (1:1000, Novus Biologicals, NB100-2331).
For Iba1 immunohistochemistry we used a biotinylated secondary antibody (Vector Laboratories) followed by processing with ABC kit (Vector Laboratories) and development with 2 mM diaminobenzidine (Sigma, USA) and 0.5 mM H_2O_2 in 0.1 M Tris buffer. Sections were put on gelatin-coated slides, air-dried overnight, dehydrated in graded solutions of ethanol, incubated in the Congo red working solution for 10 min, washed 2 times with ethanol 95% and then 2 times with ethanol 100% for 3 min each. After that, samples were cleared in xylene, and mounted with Canada balsam.
For immunofluorescence, sections were incubated with anti-rabbit Alexa 488 (Invitrogen) and anti-mouse Alexa 555 (Invitrogen), put on gelatin-coated slides and mounted with PVA-DABCO (Sigma-Aldrich, USA).

Image acquisition

For immunohistochemistry, images from each section were obtained using a 518CU Micrometrics camera attached to a Nikon Eclipse E200 microscope. For immunofluorescence, a Nikon Eclipse E80 confocal microscope was used.

Iba1 immunoreactive area

On each image obtained under a 100x magnification, the area of the stratum radiatum and hilus was delimited using the Optimas 6.5 software (Media Cybernetics). Iba1 immunopositive area was calculated as the ratio between the positive area and the corresponding subfield area, using a user-defined threshold. The area occupied by Congo red staining was filtered using Photoshop software (Adobe Systems Inc. San Jose, CA) to prevent parameter overestimation.

Microglial density

Microglial density was estimated using a randomly placed $6x10^5$ μm^3 counting probe on each hippocampal subfield. A minimum of 100 cells per animal was counted.

Microglial distribution

The distribution of microglia was assessed using the nearest neighbor distance (Nnd) parameter. A user-defined threshold was established where only the somas remained visible; using a plugin for ImageJ (Nnd plugin, Yuxiong Mao), the Nnd for each soma was calculated. The nearest neighbor mean distance resulted as the mean of all values obtained for each section. To evaluate the homogeneity of the cellular distribution we calculated a regularity index (RI) as the ratio between the nearest neighbor mean distance and the standard deviation within each sample (Whitney et al., 2008).

Microglial soma size

Soma size was evaluated as an indirect measure of microglial activation. Microphotographs from randomly chosen individual cells were obtained, the soma delineated and its surface quantified using ImageJ software. At least 50 cells were quantified for each animal.

Microglial activation

Four distinctive microglial phenotypes (ramified, intermediate, reactive and ameboid) were discriminated in the hippocampus of PDAPP-J20 mice. The ramified morphology is generally associated with non-activated microglia and was identified by a small round soma and multiple thin processes. Intermediate phenotype encased a series of modifications to the former, like a larger or more elongated soma and thicker processes. Reactive microglia showed thicker and less numerous processes together with a larger and less defined soma. Ameboid morphology presented a large soma, very few or absence of processes and was almost exclusively found near amyloid plaques. Using a randomly placed $6x10^5$ μm^3 counting probe, the proportion of each phenotype was analyzed. At least 100 cells were classified on each animal.
Microglial activation was quantified using an activation score which results from the sum of the multiplication of each morphology proportion by a factor as follows: 0, 1, 2 and 3 for ramified, intermediate, reactive and ameboid (phagocytic type) morphology respectively.

Intracellular deposits and autophagy evaluation

Percentages of GFAP+LC3+/GFAP+ and Iba1+ubiquitin+/Iba1+ cells were quantified using randomly placed 0.026 mm^2 counting frames on confocal images of the CA1 region of the hippocampus under a 20X objective. Plaque-associated cells were quantified placing the frame on amyloid deposits while in non plaque-associated cells the frame was placed at least 50 µm away from any deposit. A minimum of 100 cells was counted per animal.

Astrocyte number and complexity evaluation

The number of GFAP+ cells was quantified in CA1 subfield using a modified version of the optical disector method as described previously (Beauquis et al., 2014). Confocal images of GFAP immunofluorescence were acquired from stratum radiatum and lacunosum moleculare in coronal brain sections, using a 40X air objective. Serial images were obtained along the Z axis (0.65-µm steps) to generate three-dimensional reconstruction (Z-stack) using ImageJ software. Density of GFAP+ cells (number of cells/unit of volume) was quantified using a randomly placed 0.0024 mm^3 counting probe. A minimum of 100 cells was counted per animal and volume (V) of the analyzed regions was estimated using the Cavalieri principle on serial sections using the formula:

$$V = T \sum A$$

Areas (A) were measured using Optimas image analysis software and the T value was obtained by multiplying the number of sections by the distance between planes. Complexity of GFAP+ astrocytes was calculated as the ratio between cell surface and volume. Both parameters were estimated on three-dimensional reconstructed images obtained from confocal Z-stacks using ImageJ software. Cells entirely located inside the analyzed sections- and not overlapping with other cells or blood vessels- were considered for counting. At least 10 cells (randomly selected) evenly distributed across sections were analyzed per animal. A threshold was applied to images to exclude eventual unspecific staining prior to binarization. Cell surface (S) was estimated using the formula:

$$S = A_1 + A_n + \frac{d}{2}(P_1 + Pn) + d\sum_{i=2}^{n} p_i$$

Where A_1 ... A_n and p_1 ... p_n are the area and perimeter, respectively, of each image from the Z-stack and d represents the distance between sections. This formula was already used and reported by our group (Beauquis et al., 2014) and is a modified version of the previously described by Chvátal et al (Chvatal et al., 2007). The formula assumes that the progression of cell area and perimeter across adjacent images of the Z-stack is linear between cell edges (see Supplementary

Fig 1).The volume of individual GFAP+ cells was estimated using the Cavalieri principle as previously described.

Cell culture

Rat astrocytoma C6 cell line (ATCC CCL-107), originally derived from an N-nitrosomethylurea-induced rat brain tumor (Benda et al., 1968) was kindly provided by Dr. Zvi Vogel (Weizmann Institute of Science, Rehovot, Israel) to Dr Kotler. C6 cells were maintained in DMEM supplemented with 10% heat- inactivated FBS (Richet, Buenos Aires, Argentina), 2.0 mM glutamine, 100 units/ml penicillin, 100 µg/ml streptomycin and 2.5 µg/ml amphotericin B. Cells were cultured at 37°C in a humidified atmosphere of 5% CO_2- 95% air, and the medium was renewed three times a week.

Plasmids and Transfection

The pCI-neo mAtg5^{WT} and mAtg5^{K130R} expression plasmids were kindly provided by Dr. Noburu Mizushima (University of Tokyo, Japan) and Tamotsu Yoshimori (Osaka University, Japan) to Dr Kotler. For transfections, C6 cells were seeded on poly-D- lysin coated coverslips in 24- well plates at a density of $8x10^3$ cells/well and allowed to grow for 48h until 50-60% confluence. Transfection complexes were prepared in serum-free media in a ratio polyethyleneimine :DNA 3.75:1 (1 µg plasmid per well). Mixtures were vortexed, incubated 10 min at RT and then drop-wise added to the cells in serum media. After 5h, media was renewed. Treatments were conducted at 24h post-transfection.

MTT reduction assay

3-(4,5- dimethyl-thiazol-2-yl)-2,5-diphenyl-tetrazolium bromide (MTT) reduction assay was carried out according to the protocol previously described (Mosmann, 1983) with slight modifications. Briefly, after transfection and exposure to Aβ1-42, cells grown on 96- well plates were washed with PBS and incubated with MTT 0.125 mg/ml in culture media for 90 min at 37°C. Then, the product formazan was solubilized in DMSO and absorbance was measured at 570 nm with background subtraction at 655 nm in a BIO-RAD Model 680 Benchmark microplate reader (BIORAD laboratories, Hercules, CA, USA). The MTT reduction activity was expressed as a percentage of cell transfected with empty vector and treated with vehicle.

Aβ1-42 exposure and immunoflourescence

C6 cells were transfected with the empty vector or a construct of overexpression for mAtg5 wild type, or mutated non-functional mAtg5. Cells were exposed during 20 h to 0.5uM Aβ1-42 peptide (Sigma) previously incubated during 72h with distilled water at 37ºC to allow fibrils formation.
After exposure, cultures were washed twice with PBS, fixed with 4% paraformaldehyde/ 4% sucrose in PBS 30 min at RT and washed five times with PBS. Fixed samples were permeabilized with Triton X-100 0.25% in PBS (10 min at RT), washed 3 times with PBS and blocked with 1% BSA in PBST (Tween 20 0.1% in PBS) overnight at 4°C. Coverslips were incubated with a solution of goat anti-LC3 (Santa Cruz Lab) 1:100 and mouse anti-Aβ (clone 4G8, Covance) 1:1000 for 1h, washed 3 times with PBS and incubated with a solution of Alexa 488 donkey anti-goat (Life Technologies) 1:1000 in 1% BSA in PBST; 1 h. After 3 washes with PBS, samples were incubated with Alexa 555 goat anti-rabbit (Life Technologies) 1:1000, 1 h. Finally, coverslips were washed three times with PBS and mounted with PVA-DABCO (Sigma-Aldrich, USA). Representative images were obtained by Nikon Eclipse E80 confocal scanning laser microscope (Nikon Instech Co., Ltd., Karagawa, Japan). Negative controls were performed by incubating samples under the same conditions without one or both primary antibodies (data not shown).

LC3- and Aβ-positive cell density

Confocal Images from C6 cell culture were obtained under a 60x objective and a user-defined threshold was applied to consider only cells with LC3+ vesicles. The number of cells containing vesicles per unit of area was determined in at least 4 images per group. The same procedure was applied to measure the density of cells containing intracellular Aβ. As the focal plane was considered to detect autophagic vesicles, extracellular Aβ fibrils were not observed in these images.

LC3- Aβ co-localization index

Manders' overlap coefficient (R) was calculated employing the intensity correlation analysis plug-in for ImageJ software with subtraction of the mean value plus 2x the standard deviation of the background. At least 30 cells per group, randomly selected, were considered for co-localization analysis

Electron microscopy

Mice were anesthetized as previously mentioned and perfused with 2.5% glutaraldehyde in PB pH 7.4. After euthanasia, brain sections containing hippocampus ($1mm^3$) were incubated during 4 h in the same fixative solution at 4ºC and washed in PB. Sections were then postfixed in 1% osmium tetroxide during 1 h at 4ºC, washed with distilled water and incubated with 2% uranyl acetate for 2 h. After dehydration, sections were embedded in Durcupan. Thin sections (0.5 µm) were first analyzed by light microscopy to select areas of interest. Ultrathin sections (0.09 um) were mounted on regular grids and stained with uranyl acetate and lead citrate before EM observations in a Zeiss 109 Electron microscope.

Statistical analysis

Data are expressed as mean ± SEM. Analyses were performed under blind condition to genotype, age or treatment. Statistical analyses were performed using unpaired Student's t test, two-way ANOVA applying Bonferroni's or Tukey's post hoc test, repeated measures (RM) ANOVA and orthogonal contrasts. Two-way ANOVA applying Bonferroni's post hoc test were done using Prism 3.02 (GraphPad Software Inc.) while Info-Stat software (Universidad Nacional de Córdoba, Argentina) was used for ANOVA applying Tukey's post hoc test and orthogonal contrasts. In all statistical analysis, the required assumptions for each test were verified and significant differences were considered at the 5% level and represented as *P* values ($P<0.05$). Error bars in graphics represent the standard error.

RESULTS

The hilus of the dentate gyrus as potentially vulnerable zone in AD mice

The dynamic of plaque deposition was studied in the hippocampus of PDAPP-J20 mice, model of AD, employing Congo red staining (Fig 1A). Amyloid plaque-covered area was quantified in CA1 stratum radiatum and in the hilus of the dentate gyrus from 5, 9, 15 and 20 month-old (m) AD mice (Fig 1B). At 5 m, very few or no detectable deposits were found in the brain. At 9 m the hilus presented a higher plaque load (5 times) than stratum radiatum (0.56 ± 0.16 % vs. 0.089 ± 0.046 %). At 15 m the plaque load in the hilus represented around 2.5% of the analyzed area being significantly higher than in stratum radiatum. At 20 m, the plaque load increased compared to 15 m in both subfields but the plaque deposition was still higher in the hilus ($P<0.001$).

Microglia activation occurs prematurely and firstly in the hilus in PDAPP mice

Figure 2A shows Iba1+ microglial cells in the hippocampus from 15 m adult PDAPP mice. Even if the distribution of microglia was highly extended as expected, many cells were found in close association to amyloid plaques (stained with Congo red). The Iba1 immunoreactive area was measured within the stratum radiatum and the hilus subfields from 3, 9 and 15 m NTg and Tg mice (Fig 2B). Transgenic mice exhibited a significant increase in this parameter in the hilus from 9 and 15 m while no changes were detected in the stratum radiatum at any age. Results concerning the density of microglial cells followed the same pattern; more Iba1+ cells were counted in the hilus from 9 and 15 m Tg mice reaching 50 and 100 % increments respectively compared to age-matched controls while no changes were detected in the stratum radiatum (Fig 2C). The activation degree of microglia was explored using a morphological score ranging from 0 to 3 on Iba1+ cells, as it is shown with representative images in Fig 3A. Ramified microglia (score 0) showed typically resting phenotype, characterized by regular soma and thin processes. Intermediate (score 1) corresponded to cells with enlarged soma and moderate labelled processes, while score 2 corresponded to reactive cells with diffusely labelled soma and shorter processes The ameboid phenotype, often found near amyloid plaques, classically matched with cells having ovoid soma and few short processes if any. At 3 m, the microglial activation score was significantly higher in the hilus from Tg mice compared to controls, increasing at 9 and 15 m whereas in the stratum radiatum the difference was found from 9 m onwards. In the NTg group no differences were detected in either subfield (Fig 3B). Microglial soma size was measured in order to complete the characterization of the activation profile. In the hilus, the soma of Iba1 labeled cells in AD mice was already larger than in controls at 3 m. In addition, this parameter exhibited a moderate but continuous increase at 9 and 15 m while in the stratum radiatum this difference was only considerable at the oldest age explored. Again, the NTg group showed no important changes in microglia soma size regardless age and subfield considered (Fig 3C).
Figure 3D shows the proportion of each activation state of microglial cells in both hippocampal subfields during adulthood (from 3 to 15 m) in Tg and NTg mice. In the hilus, at early stages, there is an important presence of the intermediate state in detriment of ramified phenotype in AD mice compared to controls. At 9 m, the situation evolves with a participation of reactive cells and a modest proportion of ameboid glia. In older Tg mice, this last phenotype increases its proportion while the ramified microglia represents only a minor contribution. In the stratum radiatum, at 3 m in AD mice an increase of the intermediate category was detected, in detriment of ramified phenotype, mostly found in age-matched NTg group. At 9 m there is an incipient contribution of reactive cells that become more evident al 15 m, when a low proportion of cells in the phagocytic category was added. Ameboid phenotype markedly increases at 15 m almost exclusively in the hilus (39.24±8.86% vs 7.50±3.18%, hilus vs. radiatum respectively), probably related to the increment of plaque density. On the other hand, the NTg group showed only a moderate increment on intermediate phenotype proportion at 15 m in both subfields, as expected, taking into account the changes in this cell type through normal brain (Hefendehl et al., 2014).

Loss of regular spatial microglial distribution in the hippocampus of young AD mice, sign of incipient reactivity

Additionally, the regularity index was studied in order to discern if the spatial distribution of microglia was altered as a sign of early activation in the hippocampus of AD mice at 3 m (Fig 4A). In hilus and radiatum a significant reduction of this index was noticed respect to controls. The nearest neighbor distance represents a sensitive measure of loss of homogeneous distribution already reported in the literature (Hefendehl et al., 2014) that could be associated to microglial activation. Shorter distances between cells are directly associated with cell movement or recruitment. Comparing with NTg mice, in the hilus and stratum radiatum from young AD mice the mean distance with the nearest Iba1+ cell was appreciably smaller. As it is shown in Fig 4B, in PDAPP mice, at 3 m a greater percentage of cells had its nearest neighbour at 10 or 15 µm from the soma center compared to controls.

Astroglia in close association to deposits shows altered autophagic flux

In AD, the inflammatory reaction in the hippocampus involves the active participation of micro- and astroglia. In young Tg mice at pre-plaque stage, when no deposits were visualized, the density of GFAP+ cells in the hilus increased compared with age-matched control group (Fig 5A). In the stratum radiatum this number was decreased compared to the NTg group, as we have previously reported (Beauquis et al., 2013). In that study, we explored the effect of an enriched environment on GFAP+ cell morphological changes distinguishing two subpopulations of astrocytes: those associated (PA) or not associated to amyloid plaques (NPA). Here, in addition, at plaque stage, we investigated the astroglial density, the cell surface, the cell volume and the surface/volume ratio - index of complexity- at 9 and 15 m of age (Fig 5C-F). At these age points the plaque load was especially high in the hilus region as it was mentioned. Due to this fact and the relative small hilar area, NPA astrocytes were difficult to discriminate. Then, the glial morphological parameters presented in Fig 5C-F correspond to stratum radiatum region. No differences were found regarding GFAP+ cell density at 9 or 15 m between Tg and control mice. At 9 and 15 m, the GFAP+ cell surface of PA astrocytes was significantly larger than the area corresponding to NPA cells or to astrocytes from NTg mice (Fig 5D). In Fig 5E the cell volume analysis is shown. While no changes in this factor were detected in astrocytes from NTg or Tg NPA groups, a remarkable volume increase (near to 150 %) was evident in Tg PA astrocytes at 9 and 15 m. In Tg mice, the cell complexity index (surface/volume) indicated a complexity loss at 9 and 15 m in PA astrocytes. GFAP+ cells from NTg or Tg NPA groups exhibited high homogeneity concerning complexity (Fig 5F).

To test if the autophagy pathway could be involved in the potential astrocytic APP-derived peptides degradation, we did a co-localization study and confocal analysis employing LC3/GFAP labeling in the hippocampus of AD and control mice (Fig 6A). Hippocampal astrocytes from control mice and NPA astrocytes from 9 m Tg did not show positive labeling for LC3 whereas in Tg mice at 15 and 20 m, only around 10 % of NPA GFAP+ cells co-localized with the specific marker LC3.

In contrast, at 15 m, more than 50 % of PA astrocytes were GFAP/LC3 + in the stratum radiatum. However, this important increase at 15 m in the co-localization rate was not noticed later, at 20 m, where only around of 20 % of GFAP+ PA cells was also LC3+ (Fig 6C). Representative images from the co-localization study between GFAP and p62 are shown in Fig 6B. Some p62+ deposits are located close to plaques. However, confocal analysis did not show co-localization with GFAP+ cells, suggesting that p62 might correspond to other cell type, i.e. activated microglia surrounding amyloid deposits.

Electron microscopy allowed us to recognize a glial cell -located near dystrophic neurites- exhibiting double membrane dense vesicles (autophagosomes like) (Fig 6J), in addition to several pathological hallmarks as the presence of dystrophic neurites (6G,I) or a highly edematized astrocyte in intimate contact with a blood vessel (6H) .

Microglia surrounding amyloid deposits is ubiquitin+ and p62+

Following the hypothesis that microglia actively reacts against amyloid deposits in AD brains involving cytoplasmic protein degradation processes, we studied Iba1/ubiquitin co-localization by confocal microscopy analysis in PDAPP mice. In this strain, two cell subpopulations were distinguished: microglial cells associated (PA) or not associated to plaques (NPA). In Fig 6D, images correspond to immunofluorescence for ubiquitin+Iba1+ cells surrounding amyloid plaques. This co-localization was quantified in the stratum radiatum in the different experimental groups as it is shown in Fig 6F. At 9, 15 and 20 m the percentage of co-localization was significantly higher in PA Iba1+ cells compared with NPA cells from Tg mice and NTg group. The proportion of Iba1+Ubiquitin+/Iba1+ was near to 30 % and no important changes were detected at ages between 9 and 20 m in PA subpopulation. Fig 6E illustrates the co-localization study between Iba1 and p62. The merged image shows the unambiguous presence of cytoplasmic p62 in Iba1+ cells nearby the amyloid deposit.

Aβ1-42 peptide stimulates autophagic vesicles formation in rat astrocytoma cells

We performed an *in vitro* experiment to confirm the involvement of autophagy in amyloid peptide processing in astrocytes, using the rat astrocytoma C6 cell line.

Taken into account the key role of Atg5 in the autophagic process (Mizushima et al., 1998) we applied a genetic strategy transfecting C6 cells with an empty vector (EV) or overexpressing a mutated non-functional Atg5 ($ATG5^{K130R}$), and the corresponding WT control ($ATG5^{WT}$). After exposure to fibrillar Aβ1-42 peptide, we found amyloid content positive for 4G8 staining inside cultured cells (Fig 7A). Cell viability was measured in these groups by MTT assay (data not shown). $ATG5^{K130R}$-transfected cells showed a subtle decrease (6.5%) in viability respect to control. No significant differences were detected among other groups.

Manders' coefficient was applied to know the degree of overlapping between amyloid content revealed by 4G8 marker and LC3 in C6 cells exposed to Aβ1-42 peptide, in order to determine if the internalized amyloid was forming part of autophagosomes. Our results showed high co-localization in cells with intact or promoted autophagy (EV or $ATG5^{WT}$ vector, 0.56±0.03 and 0.49±0.04 respectively). On the other hand, in the case of defective autophagy (cells expressing the $ATG5^{K130R}$) this coefficient exhibited a decrease near to 46% (Fig 7B)
The M1 and M2 coefficients largely confirmed this concept, being M2 an indicator of the proportion of the green signal (LC3) coincident with a signal in the red channel (4G8) over its total intensity. In C6 cells with impaired autophagic process, we found a reduction near to 60% in M2 coefficient compared with control cells. M1 showed an upraised consistency between experimental groups (EV 0.89±0.01, $ATG5^{WT}$ 0.83±0.02, $ATG5^{K130R}$ 0.82±0.03).

The number of Aβ + cells significantly decreased when C6 cells were transfected with $ATG5^{K130R}$, where autophagy was impaired (Fig 7C). Immunofluoresce against LC3 showed diffuse labeling in controls group or intense vesicular signal for autophagosomes in case of autophagic induction. We verified a marked increment of cells expressing LC3+ vesicles after exposure to Aβ1-42 peptide in C6 cells transfected with EV or $ATG5^{WT}$. In contrast, the number of C6 transfected with $ATG5^{K130R}$ containing LC3+ vesicles did not change from EV-vehicle group (Fig 7D).

The kinetics of plaque deposition, microglial reactivity, astrocyte changes and protein degradation process involving glial cells in the hippocampus of Tg PDAPP mice from early to advanced stages of the disease are illustrated in Fig 8.

DISCUSSION

Aβ accumulation was classically postulated as the first and necessary step in the amyloid cascade hypothesis. However, soluble or small oligomeric forms of Aβ have been associated with deleterious actions in the brain, promoting disease progression through synaptic dysfunction, neuronal loss and/or neurodegeneration and behavioral deficits (Kim et al., 2003; Lacor et al., 2007; Lue et al., 1999).
In a previous work we described several changes in neuronal and astroglial populations occurring early in the hippocampus of 5 month-old PDAPP-J20 transgenic mice, before amyloid plaque deposition but when incipient and relatively low levels of soluble Aβ 1-40 and 1-42 peptides are detectable in brain homogenates (Beauquis et al., 2014). Astrocytes located around amyloid plaques showed morphological alterations and significantly increased cell volume. Those astrocytes located away from Aβ also exhibited changes in GFAP labeling but, on the contrary, indicative of cell atrophy. Other AD models, including 3xTg carrying APP, presenilin and Tau mutations showed coincident results (Verkhratsky et al., 2014a). Besides astroglia, microglia has been implicated in the hippocampal pathology of both in AD patients and animal models.

In the present study, we examined the progression and dynamics of microglial changes in PDAPP-J20 mice from 3 until 20 m of age as well as plaque deposition kinetics. In the hippocampus of this mouse model, Congo red labeled-senile plaques were detected at 9 m primarily in the hilus of the dentate gyrus and at 15 m in the stratum radiatum. Immunohistochemical study employing 4G8 antibody yielded the same results as Congo Red staining, but we chose the latter because small or incipient Aβ deposits were more precisely detected. No visible deposits were found in NTg mice irrespective of the age. Plaque formation occurred in an age-dependent manner in Tg mice. At 20 m the plaque load was substantially high in the hippocampus and we observed that was consistently more conspicuous in the hilus region than in the stratum radiatum. The hilus is constituted by relatively big somatostatin+ interneurons mainly sensitive to aging and a variety of insults. Loss of hilar interneurons has been associated with specific conditions such as diabetes mellitus and aging, and also with the administration of kainic acid, a specific agonist of glumatate receptors (Beauquis et al., 2006; Maia et al., 2014; Spiegel et al., 2013). Adjacent to the hilus lays the subgranular zone of the dentate gyrus a unique and restrictive brain area hosting neural progenitors that initiate adult neurogenesis. Our group and other have described a reduction in the neurogenic capability of the subgranular zone in young AD transgenic mice (Beauquis et al., 2014; Fu et al., 2014), adding evidence for a distinct vulnerability of this region.

Takahashi et al reported loss of GABAergic hilar interneurons expressing calcium-binding protein in the APP/PS1 mutant mouse, model of AD, suggesting the notion of a differential, subregion-specific susceptibility. Remarkably, a loss of calretinin – an specific calcium-binding protein-immunoreactive hilar neurons, together with a substantial gliosis within the hilus has been reported in brains of AD patients (Takahashi et al., 2010). Recently, Zlokovic´s group studied blood brain barrier breakdown by high resolution MRI analysis in living humans with Mild Cognitive Impairment. They clearly identified the hippocampus as the primary damaged structure during brain aging. In particular the dentate gyrus is mentioned as a subfield early exposed to vascular permeability (Montagne et al., 2015). Loss of vascular integrity was shown to be associated with AD progression (Lin et al., 2013).

Additionally, preliminary results from our lab showed the presence of reactive microglial cells in the hilus from C57BL/6 control mice exposed to a moderate high fat diet, suggesting an early sign of central inflammation in the same subfield (Vinuesa et al., unpublished data).

Taken together, these evidences could suggest the idea of a common primary vulnerable subzone, susceptible to a variety of insults, regardless the condition or mouse strain analyzed. Our studies showed that activated microglia can be detected firstly in the hilar region of young AD mice, well before the presence of amyloid deposits. The regularity index, an accurate measure of microglial distribution disturbances, confirmed an early sign of reactivity in the hippocampus. The hypothesis supporting that this incipient response could be associated to the initial rise in levels of detection of soluble 1-40 and 1-42 Aβ peptides -which levels are already measurable at the pre-plaque stage, as previously reported (Beauquis et al., 2014)- and to secreted inflammatory molecules by neuroglia could help to explain this fact. The source of these soluble peptides could potentially be linked to big hilar interneurons accumulating substantial amounts of Aβ, constituting another hypothesis to test.

At 9 and 15 m an increased proportion of microglia presenting activated phenotypes was observed in the hippocampus of PDAPP-J20 mice. Particularly, a relatively high proportion of ameboid microglia was present in the hilus. According to the literature, this phenotype is associated with increased phagocytic capacity, probably coinciding with M2 deactivated state (Sierra et al., 2013)

Strong evidence indicates that the amyloid apparition is related to functional microglia impairment as it was elegantly demonstrated by Krabbe and co-workers (Krabbe et al., 2013). Interestingly, we note that Iba 1+ cells in the stratum radiatum also showed an aggregated distribution, but the morphological changes related to an increased activation were more gradual and less pronounced than in the hilus.

In coincidence with other reports, using double immunofluorescence with 4G8 and GFAP antibodies, our data showed the presence of APP-related peptides apparently inside the astrocytes

located in close contact with deposits (Beauquis et al., 2013). Our *in vitro* results strongly confirmed this notion. In astrocytoma cells exposed to Aβ1-42 peptide, amyloid content was found mainly into autophagosomes. When autophagic flux was impaired -by transfection with plasmid carrying a mutated ATG5 gene-, the LC3 and Aβ overlapping degree significantly decreased.

Until now, most research related to protein degradation systems has been largely focused more on neurons than on glial cells. In the neurodegenerative condition, the neurons are frequently associated with aggregated protein accumulation, though some authors suggest that glial cells could be better equipped to maintain protein homeostasis (Jansen et al., 2014). Also, during the last decade we have learned that autophagy is clearly impaired in the AD brain. Affected regions present dystrophic neurites with an accumulation of autophagic vesicles containing undigested material (Nixon et al., 2005). In the literature, there is consistent evidence that this degradative process has neuroprotective properties, because its induction improves cognitive performance and reduces amyloid load in different animal models of AD (Spilman et al., 2010; Majumder et al., 2011). Spilman et al have shown that the inhibition of mTOR by rapamycin treatment improves cognitive performance and reduces Aβ levels in PDAPP-J20 mice (Spilman et al., 2010). In rapamycin-treated AD mice, the authors found robust LC3-labeled puncta in CA1 neuronal processes. On the other hand, there is evidence that autophagic vacuoles of neurons in which autophagy is induced are able to generate Aβ from APP (Yu et al., 2005). However, the existing information about autophagy on glial cells participating in neurodegeneration is still scarce. Interestingly, in a lysosomal storage disorder specifically induced in astrocytes, dysfunctional autophagy was reported, in association to cortical damage, suggesting a central role for astrocytic autophagic function in brain homeostasis (Di Malta et al., 2012). A recent study showed the involvement of the autophagic process in an in vitro approach using both, a microglia cell line and primary microglia cultured with β amyloid fibrils (Cho et al., 2014).

Our results show astrocyte density alteration in the hippocampus of AD mice at early stages before plaque detection. The presence of amyloid deposits is linked to important changes on this cell population. The astrocytes associated to plaques expanded their cell volume and lost complexity, symptomatic of potential dysfunction. Confocal analysis of LC3/GFAP immunolabeling evidenced the participation of the autophagic process on glial cells in close interaction with amyloid deposits. There was a clear increase of LC3 in astrocytes until 14 m but after this age it was only moderately detected on astrocytes around plaques, possibly due to the well documented aging-associated decline in autophagy (Martinez-Vicente and Cuervo, 2007). Autophagy seems to be activated and functional on GFAP+ cells without signs of substrate accumulation (p62 was not found on GFAP+ cells) and could be involved in intracytoplasmic amyloid degradation. Our electron microscopy images showed several pathological hallmarks in Tg hippocampus, including dystrophic neurites and close to them, edematized astrocytes containing typically dense autophagosomes as Figure 6G shows. This work provides evidences of autophagy occurring on glial cells surrounding amyloid deposits in a mouse model of AD. In line with this finding, our *in vitro* results support that fibrillar amyloid is able to induce autophagy on C6 astrocytes. Clearly, amyloid material is largely located inside autophagic vesicles. Hence, when autophagy is defective in C6 cells exposed to Aβ1-42 there is poor co-localization between autophagosomes and APP–derived products, suggesting that Aβ internalization involves autophagy in glia. Nielsen el at suggested that the uptake of Aβ by astrocytes seems to depend on the degree of aggregation (Nielsen et al., 2010). Even if there is substantial evidence of Aβ uptake by glial cells, their ability to degrade it is not demonstrated. Some *in vitro* evidences show co-localization between Aβ and lysosomal markers -as Lamp 1 or Lamp2- strongly suggesting the involvement of proteolytic pathways (Mandrekar et al., 2009). Moreover, a recent *in vitro* study, where neurons and glia were co-cultured with Aβ 1-42 determined the implication of degradative pathways, involving particular changes in autophagic factors in microglia (Francois et al., 2013). In line with this, we found co-localization between Iba1 and ubiquitin mostly in cells in contact with amyloid deposits in hippocampal slices from Tg mice. The presence of p62 on Iba1+ cells evidence, at advanced disease progression, a torpid autophagic flux occurring in plaque-associated microglia, in opposition to astroglia, where p62 was not detected. The phagocytic microglial dysfunction associated to Aβ presence (Heneka et al.,

2013) could be potentially linked to autophagy impairment as it was recently suggested (Cho et al., 2014).
Schematized in the Graphical Abstract /Fig 8, we show the active participation of astro- and microglia from the early beginning of the disease in the hippocampus of PDAPP mice, model of AD. Glial alterations occur first as a potential reaction to soluble Aβ peptides. Later, activated glial cells surrounding amyloid deposits could be implicated in Aβ internalization, involving altered autophagic flux.

Conclusion

Very early, both, astro- and microglial cells show signs of reactivity and the hilus of the dentate gyrus seems to be a particularly susceptible subfield to the onset of neuroinflammation. Coincidently, at least in this mouse model, amyloid deposition is predominantly and firstly found in the hilus. Afterward, the plaque load increases in other hippocampal subfield as stratum radiatum, in parallel with the progression of microglial reactivity. At advanced stages, glia could be implicated in amyloid plaque degradation, evidencing an important and novel role for glial cells involving autophagy in this disease. Moreover*, in vitro* approaches including gain and loss of autophagy function suggest that this process plays a key role in Aβ internalization/uptake in glial cells. Many aspects related to the modulation of this process need to be deeply investigated. Our data contributes to better understand the complex implication of glia on neurodegenerative progression, in particular in AD.

LEGENDS TO FIGURES

Figure 1. Amyloid plaque deposition in stratum radiatum and hilus of PDAPP-J20 mice.
(A) Representative images of Congo red-stained sections from animals of 9 and 20 months (m). Note the higher density of plaques (arrowheads) observed in the hilus compared to the CA1 region. (B) Plaque load was assessed on stratum radiatum and hilus from 5, 9, 15 and 20 month-old mice (n=5, Two-way ANOVA, Bonferroni's post hoc test *P<0.05; *** P<0.001).

Figure 2. Age-dependent increase in microglial density in the hilus of J20 mice.
(A) Image from a 15 months (m) mouse hippocampus after Iba1 immunohistochemistry and Congo red staining. Area enclosed by the white and black lines represents stratum radiatum and hilus respectively. (B) Quantification of Iba1+ area relative to total subfield area. Only the hilus of Tg mice exhibited increased immunoreactivity at 9 and 15 m. (C) Iba1+ microglial density was increased in Tg mice at 9 and 15 m only in the hilus (n=5, Two-way ANOVA, Bonferroni's post hoc test *P<0.05; **P<0.01; ***P<0.001).

Figure 3. Microglial activation is morphologically detected earlier in the hilus.
(A) A morphologic activation score (0-3) was employed where Iba1+ cells were divided into four categories (see text for description). Representative images of cell morphology for each category. (B) At 9 and 15 months (m) , Tg mice exhibited a higher activation score than NTg on both subfields, whereas at 3 m the difference was significant only in the hilus. (C) Microglia in the hilus of Tg mice showed a larger soma compared to their NTg siblings at all ages studied, whereas at stratum radiatum an increment was seen only at 15 m (n=5, Two way ANOVA, Bonferroni's post hoc test *P<0.05; **P<0.01; ***P<0.001; orthogonal contrast #P<0.05) (D) Qualitatively, Tg animals presented an age-associated increment in the proportion of the activated morphologies on both hippocampal regions.

Figure 4. Microglia of young J20 mouse shows a more aggregated distribution.
(A) Distribution of microglial cells was evaluated in stratum radiatum and hilus of 3 months (m) Tg and NTg mice using a regularity index based on the nearest neighbour parameter. The regularity of cell distribution decreased on Tg group on both subfields (n=5, Student's two tailed t test **P<0.01) (B) The analysis of nearest neighbour distances showed that Tg animals displayed a distribution shifted towards a lower distance in both subfields (n=5, Two-way RM ANOVA, Tukey's post hoc test +P<0.05).

Figure 5. Astroglial alterations before and after amyloid deposition.
(A-B) Astroglial density was quantified on stratum radiatum and hilus of 5 m Tg and NTg mice using z-stacked confocal images of GFAP+ cells. At 9 and 15 months (m) (plaque stage), plaque-associated (PA) and non-plaque-associated (NPA) astrocytes were studied. Due to the high plaque density found on the hilus at these ages, measures were done only on stratum radiatum (n=5, Student's t test *P<0.05; **P<0.01) (C) At 9 and 15 m, Tg and NTg mice had no differences in cell density. (D-E) Cell volume and surface were calculated from individual GFAP+ cells using their perimeter and area. PA astrocytes show both parameters increased compared with NPA cells. (F) Cell complexity was assessed using the surface/volume ratio. PA cells were significantly less complex compared with NPA or NTg groups (n=4, 10 cells per animal in E-F, Two-way ANOVA, Tukey's post hoc test +P<0.05; orthogonal contrast #P<0.05).

Figure 6 . Plaque-associated glia shows alterations on autophagic markers.
(A-B) Representative confocal images of GFAP/LC3 and GFAP/p62 immunofluorescences in the stratum radiatum of 15 months (m) Tg mice. Around plaques (indicated by *) LC3 was only present in the perinuclear zone of astrocytes (arrowheads). Cells containing p62 (arrows) were seen around plaques but were not GFAP+. (C) Percentage of plaque-associated (PA) and non-associated (NPA) GFAP+/LC3+ was quantified on stratum radiatum of Tg mice. At 15 m, this parameter shows a great increase in PA astroglia, being significantly higher than NPA cells. At 20 m this effect was no longer statistically significant. No co-localization was present on NTg controls. (D-E) Confocal images of Iba1/ubiquitin and p62/Iba1 immunofluorescences. Several PA microglia exhibited ubiquitin and p62 in the cytoplasm (arrowheads) (F) Percentage of PA and NPA Iba1+/ubiquitin+ microglia on stratum radiatum of Tg and NTg mice. Ubiquitin aggregates were significantly more abundant in PA microglia than in NPA or NTg cells at all ages studied (n=4, Two way ANOVA, Bonferroni's post hoc test *P<0.05;

**P<0.01; Tukey's post hoc test +P<0.05; orthogonal contrast #P<0.05). (G) Electron micrographs from the hippocampus of a transgenic PDAPP mouse showing the presence of dystrophic neurites [DN], an edematized astrocyte [A] in intimate contact with a blood vessel [BV] (H) an astrocyte containing vesicles in the vicinity of dystrophic neurites (9µm away), at low magnification (I) and the corresponding inset at high magnification focusing in the astrocytic cytoplasm where a mitochondria was identified [M] as well as the double membrane vesicle-like structures (indicated with arrowheads), suggestive of autophagosomes (J). Note that astrocytes showed in H-J, were identified by its relatively large size, clear cytoplasm and the presence of glycogen granules.

Figure 7 β-Amyloid fibrils internalization in C6 cells is dependent on autophagy.
(A) Representative confocal images of C6 cells transfected with empty vector (EV), or transfected with constructs of $ATG5^{WT}$ or $ATG5^{K130R}$ overexpression. Cells were stimulated with Aβ fibrils or vehicle during 20 hours. Arrows show aggregated LC3+ vesicles containing Aβ. Bar scale represents 20 µm. The LC3-Aβ co-localization coefficient is shown in (B) (n=30 cells; ***P<0.001 differences respect to EV-transfected cells). (C) Overexpression of $ATG5^{K130R}$ produces a decreased number of cells containing intracellular Aβ, but $ATG5^{WT}$-transfected cells have shown no changes (n=4; *P<0.05 differences respect to EV-transfected group). (D) Overexpression of $ATG5^{WT}$ increases the number of cells containing LC3+ vesicles, as expected. Moreover, treatment with Aβ causes an increment in the number of cells containing LC3+ vesicles, but this increase is absent in $ATG5^{K130R}$-transfected cells (n=4; *P<0.05; ***P<0.001 differences respect to EV-Vehicle treatment)

Figure 8/Graphical Abstract. Schematic representation of glial changes found in the hippocampus of PDAPP-J20 mice before and after plaque deposition. In each schema, a representative portion of two hippocampal subfields, the stratum radiatum (upper) and the hilus (bottom) is included. Several glial parameters are affected in the young pre-plaque mice. These changes were more pronounced and precocious in the hilus subfield. Amyloid deposition markedly aggravates the situation, promoting glia recruitment and increased reactivity. At advanced stages, astroglia increased LC3 labelling while microglia was strongly positive for ubiquitin and p62, suggesting altered autophagic activity.

Supplementary Figure 1. Astrocyte Reconstruction.
Consecutive confocal images along the Z-axis were taken from coronal brain sections processed for GFAP immunofluorescence (tissue is on X-Y plane). In the figure, images from 3 different planes are represented. Complete and randomly selected astrocytes were considered for cell surface and volume estimation. GFAP+ area (A) and perimeter (P) were measured in each image with digital software. The single cell's volume was calculated assuming that the GFAP+ area does not change along the planes between consecutives images, as shown in the figure in dark-gray. On the other hand, the single cell's total surface was calculated considering that GFAP+ areas and perimeters change linearly in the space between consecutive images, as shown by dashed lines

ACKNOWLEDGEMENTS
The authors thank Professor Juan José Lopez, PhD and Mariana Lopez Ravasio from IBCN, Facultad de Medicina UBA for electronic microscopy support, Pablo Pomata for his assistance with confocal microscopy and the personnel of the animal facility at the Instituto de Biología y Medicina Experimental (IBYME) for their help with animal care. JB, AA, MLK and FS are career investigators from Consejo Nacional de Investigaciones Científicas y Técnicas of Argentina (CONICET). PP was a doctoral fellow from ANPCYT, RMG is a post doctoral fellow from CONICET and AV and CP are doctoral fellows from CONICET.

The authors declare that no competing interests exist

BIBLIOGRAPHY

Reference List

Abramoff MD, Magelhaes PJ, Ram SJ. 2004. Image Processing with ImageJ. Biophotonics International 11:36-42.

Bansal R, Staib LH, Laine AF, Hao X, Xu D, Liu J, Weissman M, Peterson BS. 2012. Anatomical brain images alone can accurately diagnose chronic neuropsychiatric illnesses. PLoS One 7:e50698.

Beauquis J, Pavia P, Pomilio C, Vinuesa A, Podlutskaya N, Galvan V, Saravia F. 2013. Environmental enrichment prevents astroglial pathological changes in the hippocampus of APP transgenic mice, model of Alzheimer's disease. Exp Neurol 239:28-37.

Beauquis J, Roig P, Homo-Delarche F, De Nicola A, Saravia F. 2006. Reduced hippocampal neurogenesis and number of hilar neurones in streptozotocin-induced diabetic mice: reversion by antidepressant treatment. Eur J Neurosci 23:1539-1546.

Beauquis J, Vinuesa A, Pomilio C, Pavia P, Galvan V, Saravia F. 2014. Neuronal and glial alterations, increased anxiety, and cognitive impairment before hippocampal amyloid deposition in PDAPP mice, model of Alzheimer's disease. Hippocampus 24:257-269.

Benda P, Lightbody J, Sato G, Levine L, Sweet W. 1968. Differentiated rat glial cell strain in tissue culture. Science 161:370-371.

Bjorkoy G, Lamark T, Brech A, Outzen H, Perander M, Overvatn A, Stenmark H, Johansen T. 2005. p62/SQSTM1 forms protein aggregates degraded by autophagy and has a protective effect on huntingtin-induced cell death. J Cell Biol 171:603-614.

Blennow K, de Leon MJ, Zetterberg H. 2006. Alzheimer's disease. Lancet 368:387-403.

Cho MH, Cho K, Kang HJ, Jeon EY, Kim HS, Kwon HJ, Kim HM, Kim DH, Yoon SY. 2014. Autophagy in microglia degrades extracellular beta-amyloid fibrils and regulates the NLRP3 inflammasome. Autophagy 10:1761-1775.

Chvatal A, Anderova M, Hock M, Prajerova I, Neprasova H, Chvatal V, Kirchhoff F, Sykova E. 2007. Three-dimensional confocal morphometry reveals structural changes in astrocyte morphology in situ. J Neurosci Res 85:260-271.

Dantuma NP, Bott LC. 2014. The ubiquitin-proteasome system in neurodegenerative diseases: precipitating factor, yet part of the solution. Front Mol Neurosci 7:70.

de Kloet ER, Vreugdenhil E, Oitzl MS, Joels M. 1998. Brain corticosteroid receptor balance in health and disease. Endocr Rev 19:269-301.

Di Malta C, Fryer JD, Settembre C, Ballabio A. 2012. Astrocyte dysfunction triggers neurodegeneration in a lysosomal storage disorder. Proc Natl Acad Sci U S A 109:E2334-E2342.

Dubois B, Feldman HH, Jacova C, Cummings JL, DeKosky ST, Barberger-Gateau P, Delacourte A, Frisoni G, Fox NC, Galasko D and others. 2010. Revising the definition of Alzheimer's disease: a new lexicon. Lancet Neurol 9:1118-1127.

Ferrera D, Mazzaro N, Canale C, Gasparini L. 2014. Resting microglia react to Abeta42 fibrils but do not detect oligomers or oligomer-induced neuronal damage. Neurobiol Aging .

Francois A, Terro F, Janet T, Rioux BA, Paccalin M, Page G. 2013. Involvement of interleukin-1beta in the autophagic process of microglia: relevance to Alzheimer's disease. J Neuroinflammation 10:151.

Fu Y, Rusznak Z, Kwok JB, Kim WS, Paxinos G. 2014. Age-dependent alterations of the hippocampal cell composition and proliferative potential in the hAbetaPPSwInd-J20 mouse. J Alzheimers Dis 41:1177-1192.

Galvan V, Gorostiza OF, Banwait S, Ataie M, Logvinova AV, Sitaraman S, Carlson E, Sagi SA, Chevallier N, Jin K and others. 2006. Reversal of Alzheimer's-like pathology and behavior in human APP transgenic mice by mutation of Asp664. Proc Natl Acad Sci U S A 103:7130-7135.

Harrison DE, Strong R, Sharp ZD, Nelson JF, Astle CM, Flurkey K, Nadon NL, Wilkinson JE, Frenkel K, Carter CS and others. 2009. Rapamycin fed late in life extends lifespan in genetically heterogeneous mice. Nature 460:392-395.

Hefendehl JK, Neher JJ, Suhs RB, Kohsaka S, Skodras A, Jucker M. 2014. Homeostatic and injury-induced microglia behavior in the aging brain. Aging Cell 13:60-69.

Heneka MT, Kummer MP, Stutz A, Delekate A, Schwartz S, Vieira-Saecker A, Griep A, Axt D, Remus A, Tzeng TC and others. 2013. NLRP3 is activated in Alzheimer's disease and contributes to pathology in APP/PS1 mice. Nature 493:674-678.

Hsia AY, Masliah E, McConlogue L, Yu GQ, Tatsuno G, Hu K, Kholodenko D, Malenka RC, Nicoll RA, Mucke L. 1999. Plaque-independent disruption of neural circuits in Alzheimer's disease mouse models. Proc Natl Acad Sci U S A 96:3228-3233.

Jaeger PA, Wyss-Coray T. 2009. All-you-can-eat: autophagy in neurodegeneration and neuroprotection. Mol Neurodegener 4:16.

Jansen AH, Reits EA, Hol EM. 2014. The ubiquitin proteasome system in glia and its role in neurodegenerative diseases. Front Mol Neurosci 7:73.

Kim HJ, Chae SC, Lee DK, Chromy B, Lee SC, Park YC, Klein WL, Krafft GA, Hong ST. 2003. Selective neuronal degeneration induced by soluble oligomeric amyloid beta protein. FASEB J 17:118-120.

Krabbe G, Halle A, Matyash V, Rinnenthal JL, Eom GD, Bernhardt U, Miller KR, Prokop S, Kettenmann H, Heppner FL. 2013. Functional impairment of microglia coincides with Beta-amyloid deposition in mice with Alzheimer-like pathology. PLoS One 8:e60921.

Lacor PN, Buniel MC, Furlow PW, Clemente AS, Velasco PT, Wood M, Viola KL, Klein WL. 2007. Abeta oligomer-induced aberrations in synapse composition, shape, and density provide a molecular basis for loss of connectivity in Alzheimer's disease. J Neurosci 27:796-807.

Lin AL, Zheng W, Halloran JJ, Burbank RR, Hussong SA, Hart MJ, Javors M, Shih YY, Muir E, Solano FR and others. 2013. Chronic rapamycin restores brain vascular integrity and function through NO synthase activation and improves memory in symptomatic mice modeling Alzheimer's disease. J Cereb Blood Flow Metab 33:1412-1421.

Lue LF, Kuo YM, Roher AE, Brachova L, Shen Y, Sue L, Beach T, Kurth JH, Rydel RE, Rogers J. 1999. Soluble amyloid beta peptide concentration as a predictor of synaptic change in Alzheimer's disease. Am J Pathol 155:853-862.

Maia GH, Quesado JL, Soares JI, do Carmo JM, Andrade PA, Andrade JP, Lukoyanov NV. 2014. Loss of hippocampal neurons after kainate treatment correlates with behavioral deficits. PLoS One 9:e84722.

Majumder S, Richardson A, Strong R, Oddo S. 2011. Inducing autophagy by rapamycin before, but not after, the formation of plaques and tangles ameliorates cognitive deficits. PLoS One 6:e25416.

Mandrekar S, Jiang Q, Lee CY, Koenigsknecht-Talboo J, Holtzman DM, Landreth GE. 2009. Microglia mediate the clearance of soluble Abeta through fluid phase macropinocytosis. J Neurosci 29:4252-4262.

Marlatt MW, Lucassen PJ. 2010. Neurogenesis and Alzheimer's disease: Biology and pathophysiology in mice and men. Curr Alzheimer Res 7:113-125.

Martinez-Vicente M, Cuervo AM. 2007. Autophagy and neurodegeneration: when the cleaning crew goes on strike. Lancet Neurol 6:352-361.

Mizushima N, Sugita H, Yoshimori T, Ohsumi Y. 1998. A new protein conjugation system in human. The counterpart of the yeast Apg12p conjugation system essential for autophagy. J Biol Chem 273:33889-33892.

Mohamed A, Posse dC. 2011. Abeta internalization by neurons and glia. Int J Alzheimers Dis 2011:127984.

Montagne A, Barnes SR, Sweeney MD, Halliday MR, Sagare AP, Zhao Z, Toga AW, Jacobs RE, Liu CY, Amezcua L and others. 2015. Blood-brain barrier breakdown in the aging human hippocampus. Neuron 85:296-302.

Mosher KI, Wyss-Coray T. 2014. Microglial dysfunction in brain aging and Alzheimer's disease. Biochem Pharmacol 88:594-604.

Mosmann T. 1983. Rapid colorimetric assay for cellular growth and survival: application to proliferation and cytotoxicity assays. J Immunol Methods 65:55-63.

Mucke L, Masliah E, Yu GQ, Mallory M, Rockenstein EM, Tatsuno G, Hu K, Kholodenko D, Johnson-Wood K, McConlogue L. 2000. High-level neuronal expression of abeta 1-42 in wild-type human amyloid protein precursor transgenic mice: synaptotoxicity without plaque formation. J Neurosci 20:4050-4058.

Nagele RG, Wegiel J, Venkataraman V, Imaki H, Wang KC, Wegiel J. 2004. Contribution of glial cells to the development of amyloid plaques in Alzheimer's disease. Neurobiol Aging 25:663-674.

Nielsen HM, Mulder SD, Belien JA, Musters RJ, Eikelenboom P, Veerhuis R. 2010. Astrocytic A beta 1-42 uptake is determined by A beta-aggregation state and the presence of amyloid-associated proteins. Glia 58:1235-1246.

Nixon RA, Wegiel J, Kumar A, Yu WH, Peterhoff C, Cataldo A, Cuervo AM. 2005. Extensive involvement of autophagy in Alzheimer disease: an immuno-electron microscopy study. J Neuropathol Exp Neurol 64:113-122.

Pihlaja R, Koistinaho J, Malm T, Sikkila H, Vainio S, Koistinaho M. 2008. Transplanted astrocytes internalize deposited beta-amyloid peptides in a transgenic mouse model of Alzheimer's disease. Glia 56:154-163.

Ravikumar B, Vacher C, Berger Z, Davies JE, Luo S, Oroz LG, Scaravilli F, Easton DF, Duden R, O'Kane CJ and others. 2004. Inhibition of mTOR induces autophagy and reduces toxicity of polyglutamine expansions in fly and mouse models of Huntington disease. Nat Genet 36:585-595.

Roberson ED, Scearce-Levie K, Palop JJ, Yan F, Cheng IH, Wu T, Gerstein H, Yu GQ, Mucke L. 2007. Reducing endogenous tau ameliorates amyloid beta-induced deficits in an Alzheimer's disease mouse model. Science 316:750-754.

Rodriguez JJ, Olabarria M, Chvatal A, Verkhratsky A. 2009. Astroglia in dementia and Alzheimer's disease. Cell Death Differ 16:378-385.

Santos RX, Correia SC, Cardoso S, Carvalho C, Santos MS, Moreira PI. 2011. Effects of rapamycin and TOR on aging and memory: implications for Alzheimer's disease. J Neurochem 117:927-936.

Selkoe DJ. 2000. Toward a comprehensive theory for Alzheimer's disease. Hypothesis: Alzheimer's disease is caused by the cerebral accumulation and cytotoxicity of amyloid beta-protein. Ann N Y Acad Sci 924:17-25.

Sierra A, Abiega O, Shahraz A, Neumann H. 2013. Janus-faced microglia: beneficial and detrimental consequences of microglial phagocytosis. Front Cell Neurosci 7:6.

Spiegel AM, Koh MT, Vogt NM, Rapp PR, Gallagher M. 2013. Hilar interneuron vulnerability distinguishes aged rats with memory impairment. J Comp Neurol 521:3508-3523.

Spilman P, Podlutskaya N, Hart MJ, Debnath J, Gorostiza O, Bredesen D, Richardson A, Strong R, Galvan V. 2010. Inhibition of mTOR by rapamycin abolishes cognitive deficits and reduces amyloid-beta levels in a mouse model of Alzheimer's disease. PLoS One 5:e9979.

Steele ML, Robinson SR. 2012. Reactive astrocytes give neurons less support: implications for Alzheimer's disease. Neurobiol Aging 33:423-13.

Takahashi H, Brasnjevic I, Rutten BP, Van Der KN, Perl DP, Bouras C, Steinbusch HW, Schmitz C, Hof PR, Dickstein DL. 2010. Hippocampal interneuron loss in an APP/PS1 double mutant mouse and in Alzheimer's disease. Brain Struct Funct 214:145-160.

Verkhratsky A, Marutle A, Rodriguez-Arellano JJ, Nordberg A. 2014a. Glial Asthenia and Functional Paralysis: A New Perspective on Neurodegeneration and Alzheimer's Disease. Neuroscientist .

Verkhratsky A, Rodriguez JJ, Parpura V. 2014b. Neuroglia in ageing and disease. Cell Tissue Res 357:493-503.

Whitney IE, Keeley PW, Raven MA, Reese BE. 2008. Spatial patterning of cholinergic amacrine cells in the mouse retina. J Comp Neurol 508:1-12.

Wilcock DM, Gordon MN, Morgan D. 2006. Quantification of cerebral amyloid angiopathy and parenchymal amyloid plaques with Congo red histochemical stain. Nat Protoc 1:1591-1595.

Wilkinson JE, Burmeister L, Brooks SV, Chan CC, Friedline S, Harrison DE, Hejtmancik JF, Nadon N, Strong R, Wood LK and others. 2012. Rapamycin slows aging in mice. Aging Cell 11:675-682.

Wright AL, Zinn R, Hohensinn B, Konen LM, Beynon SB, Tan RP, Clark IA, Abdipranoto A, Vissel B. 2013. Neuroinflammation and Neuronal Loss Precede Abeta Plaque Deposition in the hAPP-J20 Mouse Model of Alzheimer's Disease. PLoS One 8:e59586.

Yu WH, Cuervo AM, Kumar A, Peterhoff CM, Schmidt SD, Lee JH, Mohan PS, Mercken M, Farmery MR, Tjernberg LO and others. 2005. Macroautophagy--a novel Beta-amyloid peptide-generating pathway activated in Alzheimer's disease. J Cell Biol 171:87-98.

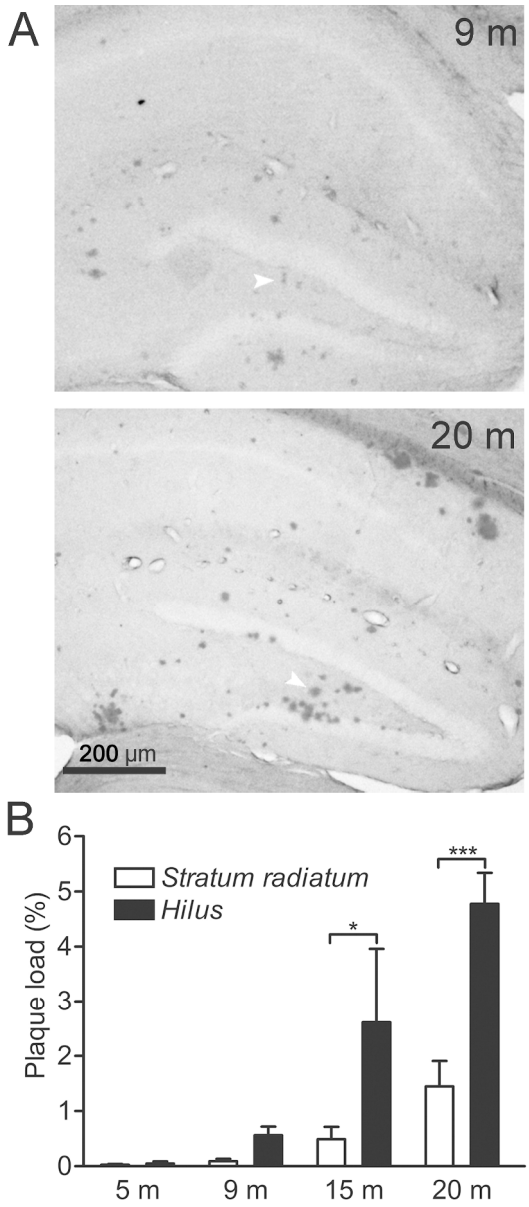

Figure 1. Amyloid plaque deposition in stratum radiatum and hilus of PDAPP-J20 mice. (A) Representative images of Congo red-stained sections from animals of 9 and 20 m. Note the higher density of plaques (arrowheads) observed in the hilus compared to the CA1 region. (B) Plaque load was assessed on stratum radiatum and hilus from 5, 9, 15 and 20 month-old mice (n=5, Two-way ANOVA, Bonferroni's post hoc test *P<0.05; *** P<0.001).

199x451mm (300 x 300 DPI)

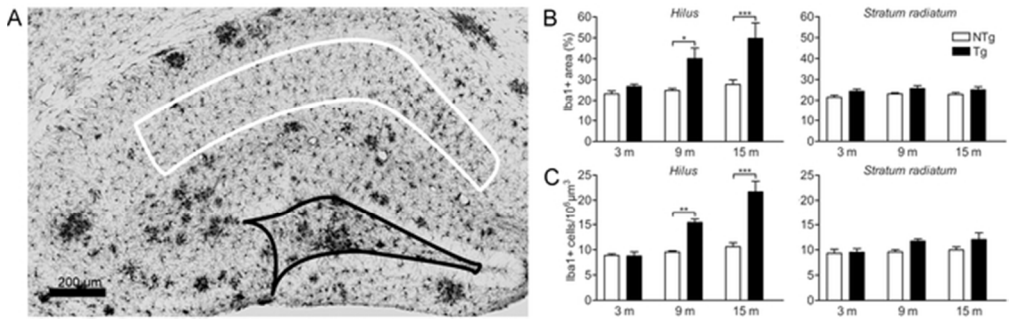

Figure2. Age-dependent increase in microglial density in the hilus of J20 mice.
(A) Image from a 15 m mouse hippocampus after Iba1 immunohistochemistry and Congo red staining. Area enclosed by the white and black lines represents stratum radiatum and hilus respectively. (B) Quantification of Iba1+ area relative to total subfield area. Only the hilus of Tg mice exhibited increased immunoreactivity at 9 and 15 m. (C) Iba1+ microglial density was increased in Tg mice at 9 and 15 m only in the hilus (n=5, Two-way ANOVA, Bonferroni's post hoc test *P<0.05; **P<0.01; ***P<0.001).

55x17mm (300 x 300 DPI)

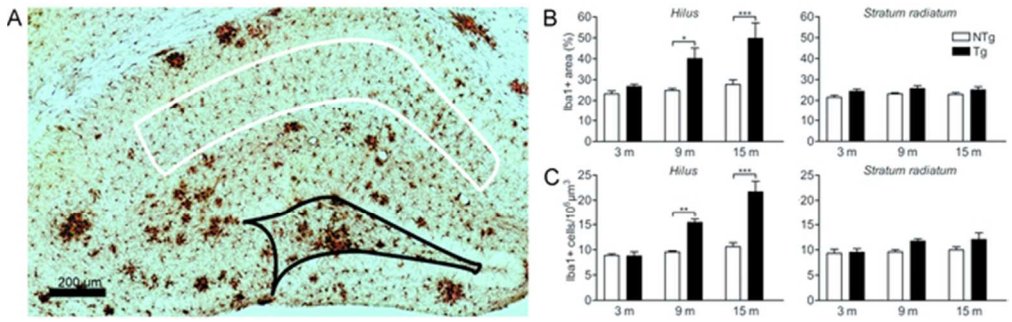

Figure 2. Age-dependent increase in microglial density in the hilus of J20 mice.
(A) Image from a 15 m mouse hippocampus after Iba1 immunohistochemistry and Congo red staining. Area enclosed by the black and white lines represents stratum radiatum and hilus respectively. (B) Quantification of Iba1+ area relative to total subfield area. Only the hilus of Tg mice exhibited increased immunoreactivity at 9 and 15 m. (C) Iba1+ microglial density was increased in Tg mice at 9 and 15 m only in the hilus (n=5, Two-way ANOVA, Bonferroni's post hoc test *P<0.05; **P<0.01; ***P<0.001).

55x17mm (300 x 300 DPI)

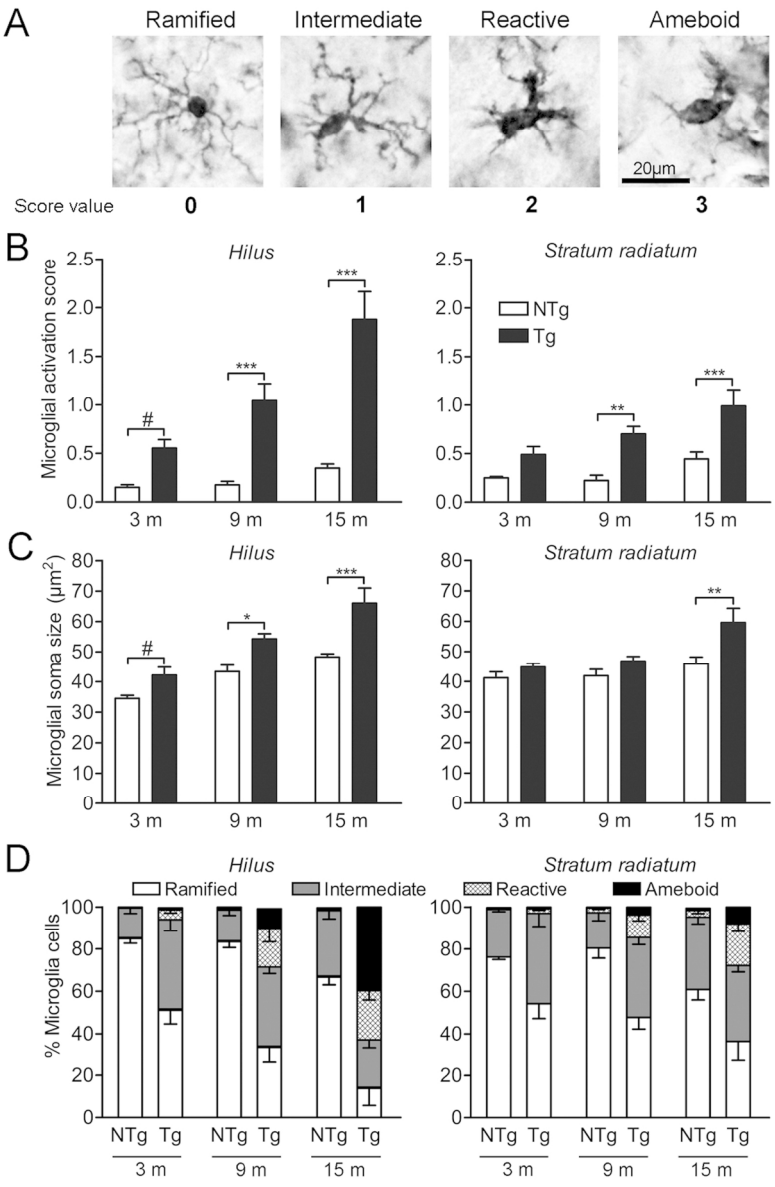

Figure 3. Microglial activation is morphologically detected earlier in the hilus.
(A) A morphologic activation score (0-3) was employed where Iba1+ cells were divided into four categories (see text for description). Representative images of cell morphology for each category. (B) At 9 and 15 m, Tg mice exhibited a higher activation score than NTg on both subfields, whereas at 3 m the difference was significant only in the hilus. (C) Microglia in the hilus of Tg mice showed a larger soma compared to their NTg siblings at all ages studied, whereas at stratum radiatum an increment was seen only at 15 m (n=5, Two way ANOVA, Bonferroni's post hoc test *P<0.05; **P<0.01; ***P<0.001; orthogonal contrast #P<0.05) (D) Qualitatively, Tg animals presented an age-associated increment in the proportion of the activated morphologies on both hippocampal regions.

134x205mm (300 x 300 DPI)

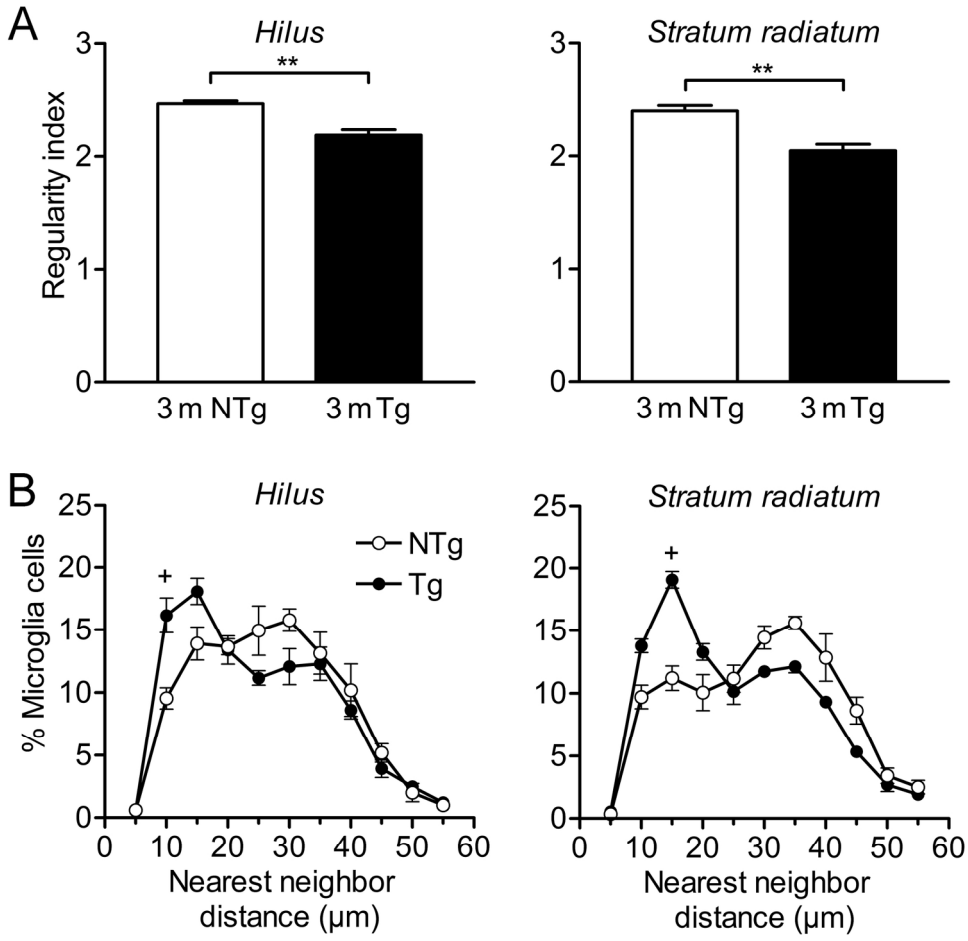

Figure 4. Microglia of young J20 mouse shows a more aggregated distribution.
(A) Distribution of microglial cells was evaluated in stratum radiatum and hilus of 3 m Tg and NTg mice using a regularity index based on the nearest neighbour parameter. The regularity of cell distribution decreased on Tg group on both subfields (n=5, Student's two tailed t test **P<0.01) (B) The analysis of nearest neighbour distances showed that Tg animals displayed a distribution shifted towards a lower distance in both subfields (n=5, Two-way RM ANOVA, Tukey's post hoc test +P<0.05).

85x82mm (600 x 600 DPI)

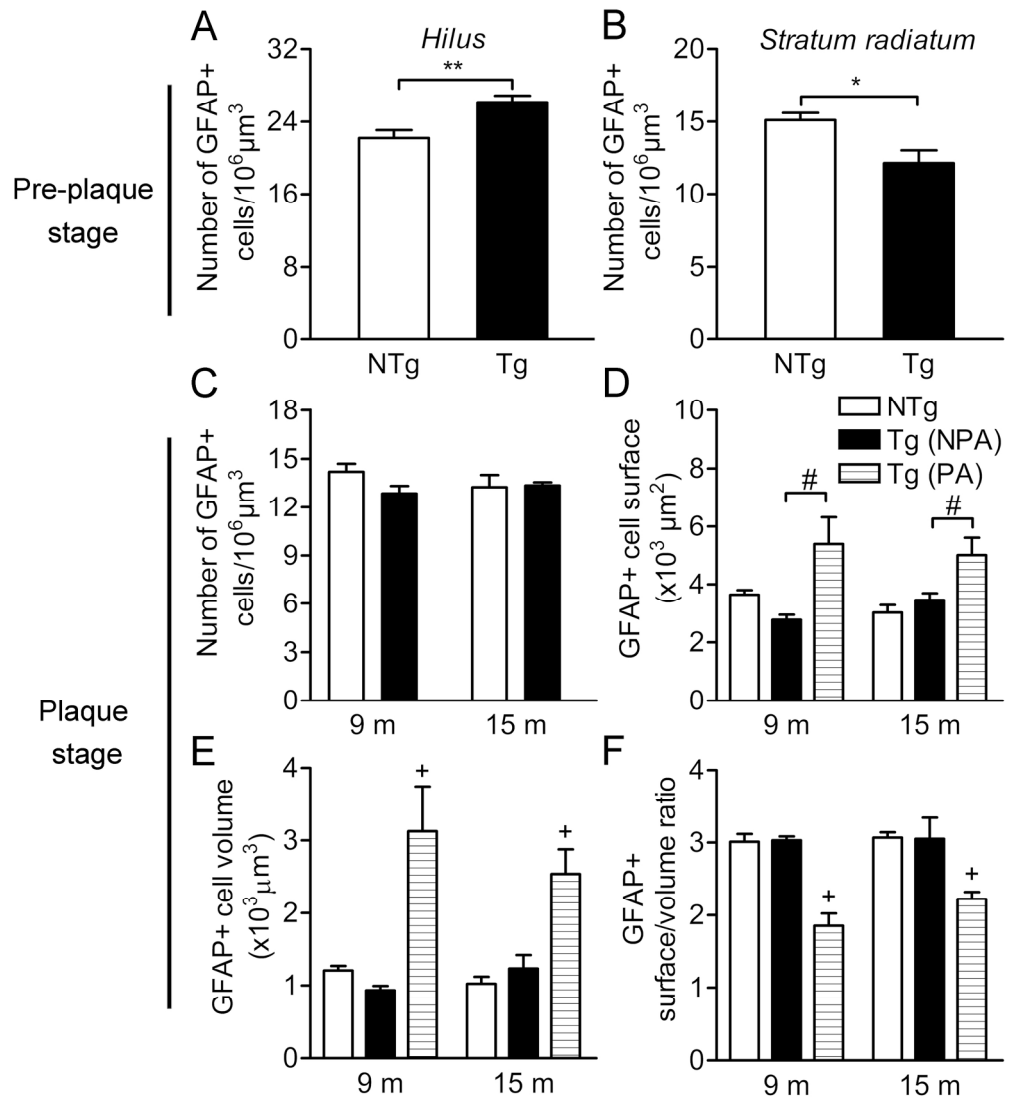

Figure 5. Astroglial alterations before and after amyloid deposition.
(A-B) Astroglial density was quantified on stratum radiatum and hilus of 5 m Tg and NTg mice using z-stacked confocal images of GFAP+ cells. At 9 and 15 m (plaque stage), plaque-associated (PA) and non-plaque-associated (NPA) astrocytes were studied. Due to the high plaque density found on the hilus at these ages, measures were done only on stratum radiatum (n=5, Student's t test *P<0.05; **P<0.01) (C) At 9 and 15 m, Tg and NTg mice had no differences in cell density. (D-E) Cell volume and surface were calculated from individual GFAP+ cells using their perimeter and area. PA astrocytes show both parameters increased compared with NPA cells. (F) Cell complexity was assessed using the surface/volume ratio. PA cells were significantly less complex compared with NPA or NTg groups (n=4, 10 cells per animal in E-F, Two-way ANOVA, Tukey's post hoc test +P<0.05; orthogonal contrast #P<0.05).

96x105mm (600 x 600 DPI)

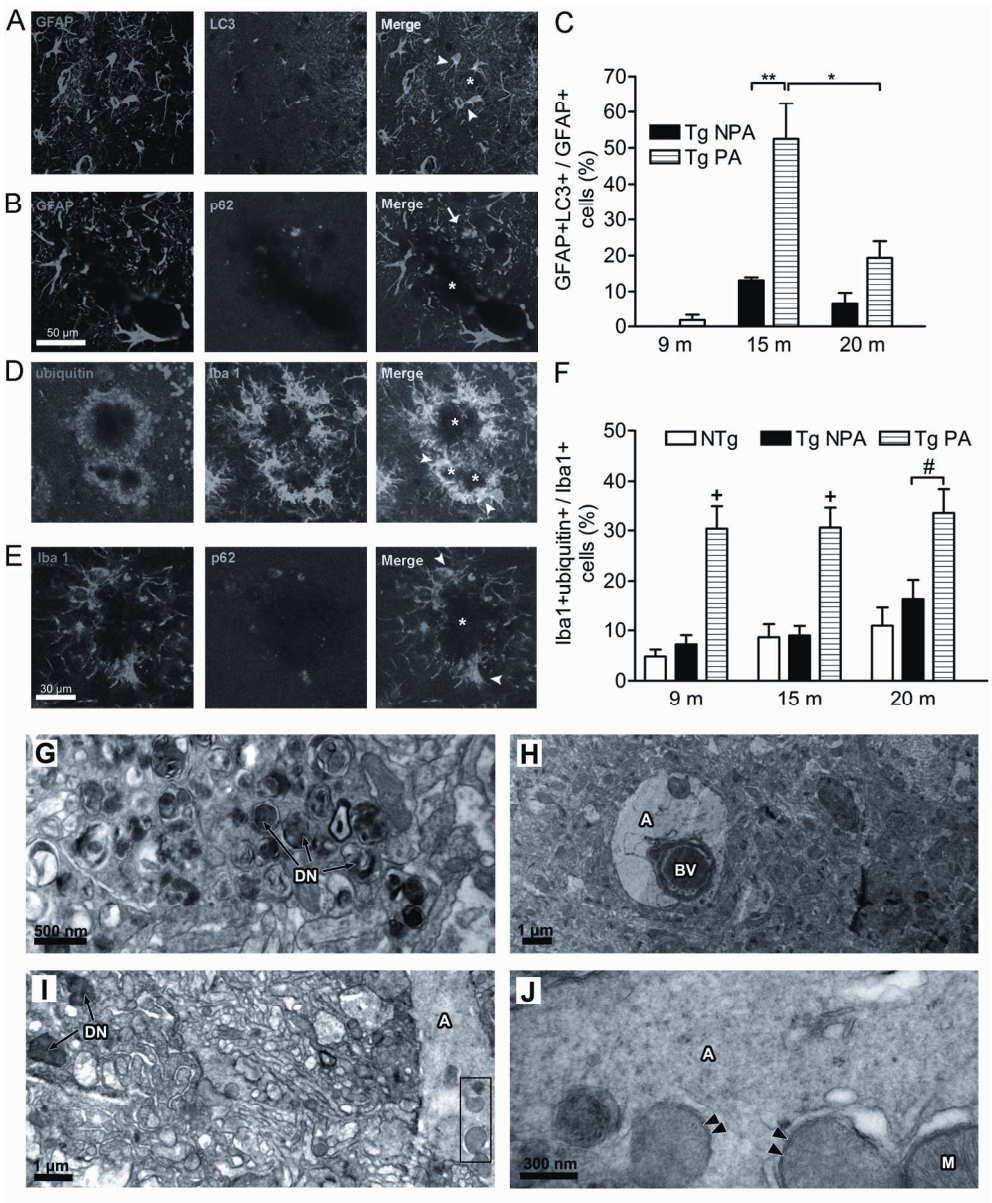

Figure 6 . Plaque-associated glia shows alterations on autophagic markers.
(A-B) Representative confocal images of GFAP/LC3 and GFAP/p62 immunofluorescences in the stratum radiatum of 15 months (m) Tg mice. Around plaques (indicated by *) LC3 was only present in the perinuclear zone of astrocytes (arrowheads). Cells containing p62 (arrows) were seen around plaques but were not GFAP+. (C) Percentage of plaque-associated (PA) and non-associated (NPA) GFAP+/LC3+ was quantified on stratum radiatum of Tg mice. At 15 m, this parameter shows a great increase in PA astroglia, being significantly higher than NPA cells. At 20 m this effect was no longer statistically significant. No co-localization was present on NTg controls. (D-E) Confocal images of Iba1/ubiquitin and p62/Iba1 immunofluorescences. Several PA microglia exhibited ubiquitin and p62 in the cytoplasm (arrowheads) (F) Percentage of PA and NPA Iba1+/ubiquitin+ microglia on stratum radiatum of Tg and NTg mice. Ubiquitin aggregates were significantly more abundant in PA microglia than in NPA or NTg cells at all ages studied (n=4, Two way ANOVA, Bonferroni's post hoc test *P<0.05; **P<0.01; Tukey's post hoc test +P<0.05; orthogonal contrast #P<0.05). (G) Electron micrographs from the hippocampus of a transgenic PDAPP

mouse showing the presence of dystrophic neurites [DN], an edematized astrocyte [A] in intimate contact with a blood vessel [BV] (H) an astrocyte containing vesicles in the vicinity of dystrophic neurites (9µm away), at low magnification (I) and the corresponding inset at high magnification focusing in the astrocytic cytoplasm where a mitochondria was identified [M] as well as the double membrane vesicle-like structures (indicated with arrowheads), suggestive of autophagosomes (J). Note that astrocytes showed in H-J, were identified by its relatively large size, clear cytoplasm and the presence of glycogen granules.

177x216mm (300 x 300 DPI)

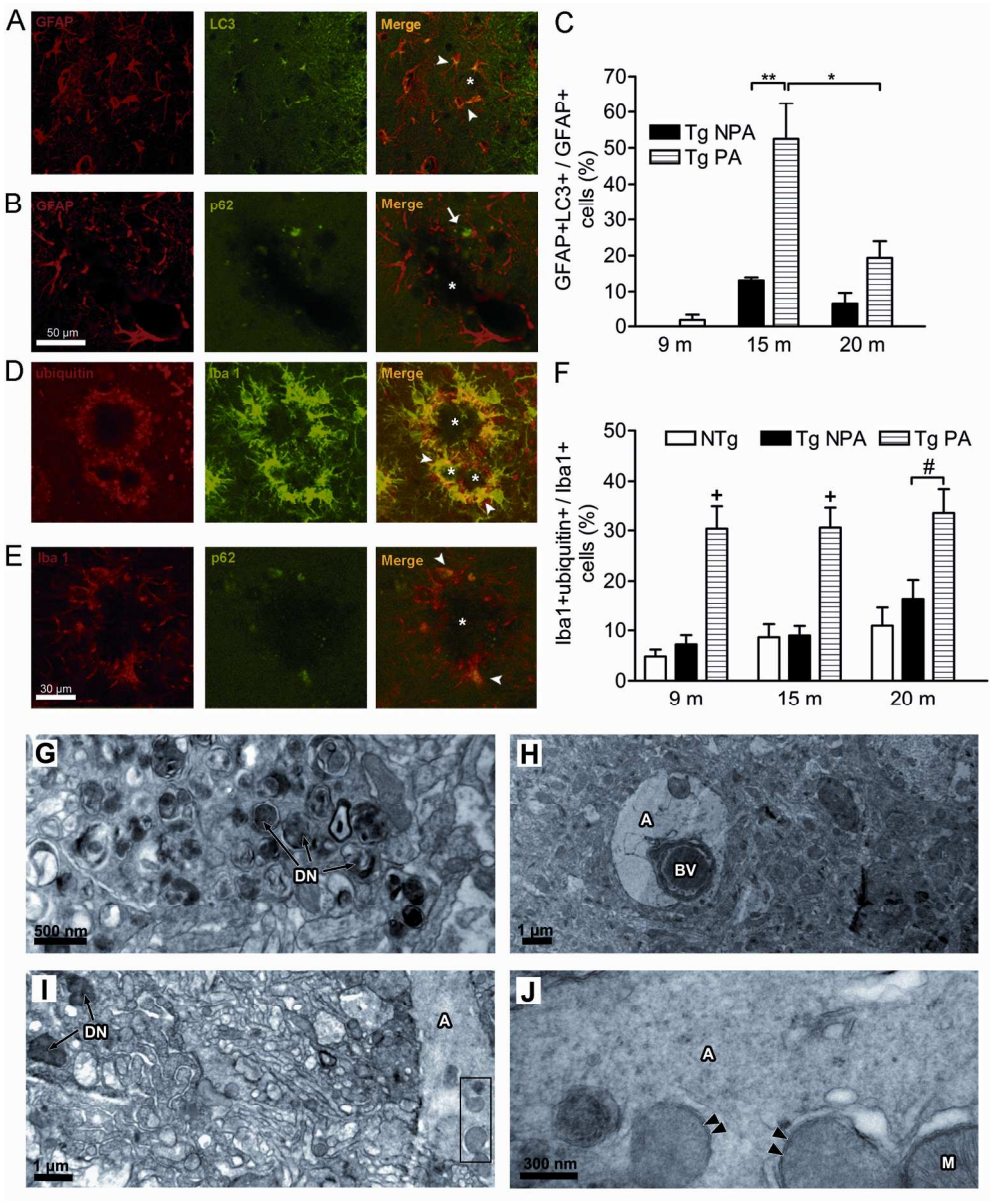

Figure 6 . Plaque-associated glia shows alterations on autophagic markers.
(A-B) Representative confocal images of GFAP/LC3 and GFAP/p62 immunofluorescences in the stratum radiatum of 15 months (m) Tg mice. Around plaques (indicated by *) LC3 was only present in the perinuclear zone of astrocytes (arrowheads). Cells containing p62 (arrows) were seen around plaques but were not GFAP+. (C) Percentage of plaque-associated (PA) and non-associated (NPA) GFAP+/LC3+ was quantified on stratum radiatum of Tg mice. At 15 m, this parameter shows a great increase in PA astroglia, being significantly higher than NPA cells. At 20 m this effect was no longer statistically significant. No co-localization was present on NTg controls. (D-E) Confocal images of Iba1/ubiquitin and p62/Iba1 immunofluorescences. Several PA microglia exhibited ubiquitin and p62 in the cytoplasm (arrowheads) (F) Percentage of PA and NPA Iba1+/ubiquitin+ microglia on stratum radiatum of Tg and NTg mice. Ubiquitin aggregates were significantly more abundant in PA microglia than in NPA or NTg cells at all ages studied (n=4, Two way ANOVA, Bonferroni's post hoc test *P<0.05; **P<0.01; Tukey's post hoc test +P<0.05; orthogonal contrast #P<0.05). (G) Electron micrographs from the hippocampus of a transgenic PDAPP

mouse showing the presence of dystrophic neurites [DN], an edematized astrocyte [A] in intimate contact with a blood vessel [BV] (H) an astrocyte containing vesicles in the vicinity of dystrophic neurites (9µm away), at low magnification (I) and the corresponding inset at high magnification focusing in the astrocytic cytoplasm where a mitochondria was identified [M] as well as the double membrane vesicle-like structures (indicated with arrowheads), suggestive of autophagosomes (J). Note that astrocytes showed in H-J, were identified by its relatively large size, clear cytoplasm and the presence of glycogen granules.

177x216mm (300 x 300 DPI)

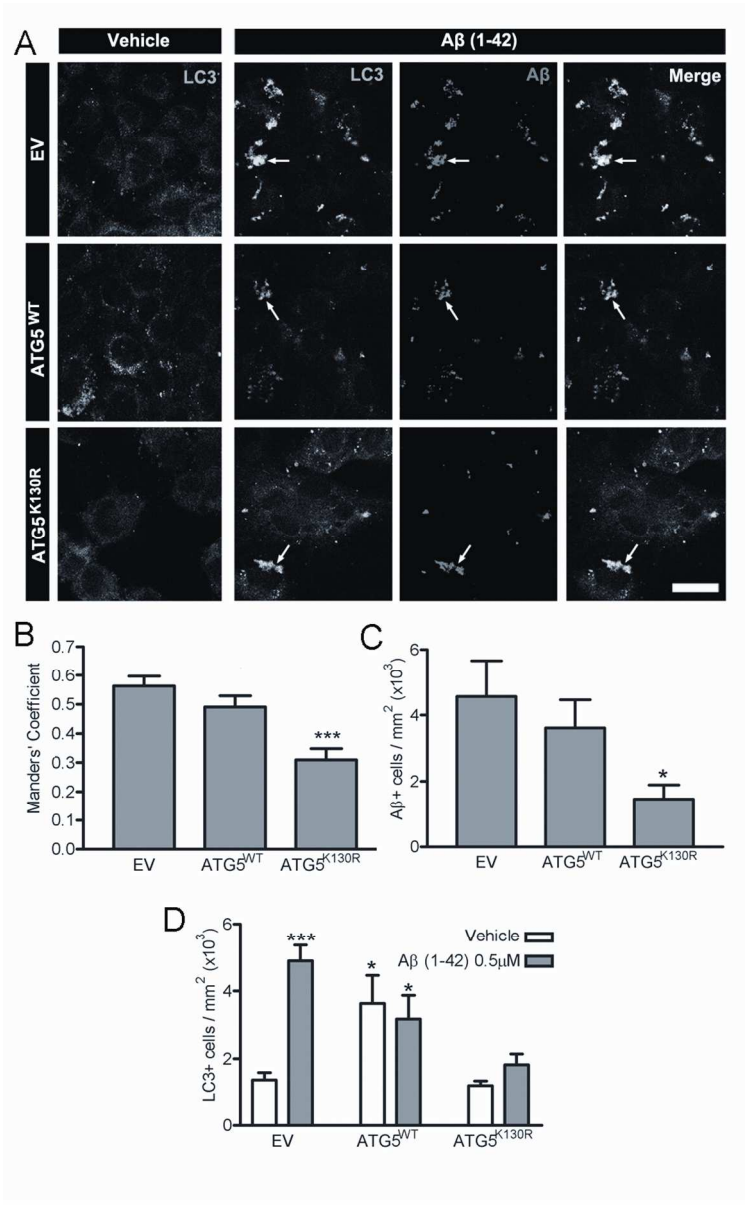

Figure 7 β-Amyloid fibrils internalization in C6 cells is dependent on autophagy.
(A) Representative confocal images of C6 cells transfected with empty vector (EV), or transfected with constructions of ATG5WT or ATG5K130R overexpression. Cells were stimulated with Aβ fibrils or vehicle during 20 hours. Arrows show aggregated LC3+ vesicles containing Aβ. Bar scale represents 20 μm. The LC3-Aβ co-localization coefficient is shown in (B) (n=30 cells; ***P<0.001 differences respect to EV-transfected cells). (C) Overexpression of ATG5K130R produces a decreased number of cells containing intracelular Aβ, but ATG5WT-transfected cells have shown no changes (n=4; *P<0.05 differences respect to EV-transfected group). (D) Overexpression of ATG5WT increases the number of cells containing LC3+ vesicles, as expected. Moreover, treatment with Aβ causes an increment in the number of cells containing LC3+ vesicles, but this increase is absent in ATG5K130R-transfected cells (n=4; *P<0.05; ***P<0.001 differences respect to EV-Vehicle treatment)

87x142mm (300 x 300 DPI)

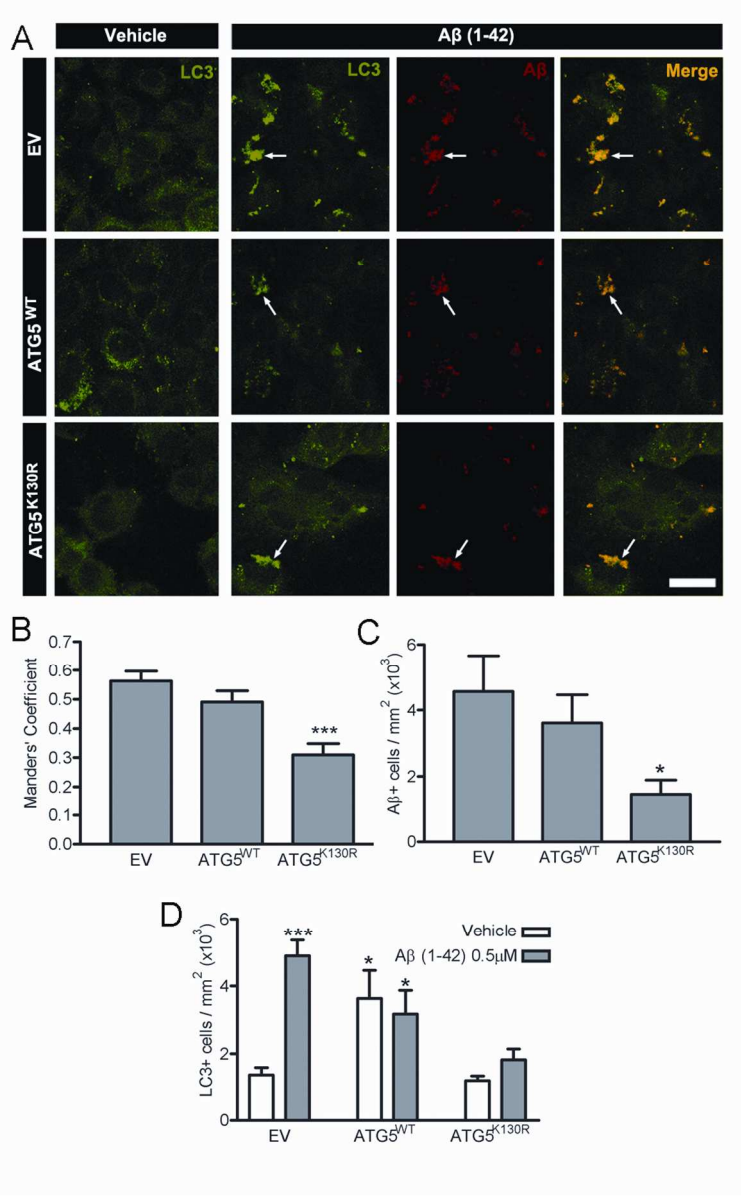

Figure 7 β-Amyloid fibrils internalization in C6 cells is dependent on autophagy.
(A) Representative confocal images of C6 cells transfected with empty vector (EV), or transfected with constructions of ATG5WT or ATG5K130R overexpression. Cells were stimulated with Aβ fibrils or vehicle during 20 hours. Arrows show aggregated LC3+ vesicles containing Aβ. Bar scale represents 20 μm. The LC3-Aβ co-localization coefficient is shown in (B) (n=30 cells; ***P<0.001 differences respect to EV-transfected cells). (C) Overexpression of ATG5K130R produces a decreased number of cells containing intracelular Aβ, but ATG5WT-transfected cells have shown no changes (n=4; *P<0.05 differences respect to EV-transfected group). (D) Overexpression of ATG5WT increases the number of cells containing LC3+ vesicles, as expected. Moreover, treatment with Aβ causes an increment in the number of cells containing LC3+ vesicles, but this increase is absent in ATG5K130R-transfected cells (n=4; *P<0.05; ***P<0.001 differences respect to EV-Vehicle treatment)

87x142mm (300 x 300 DPI)

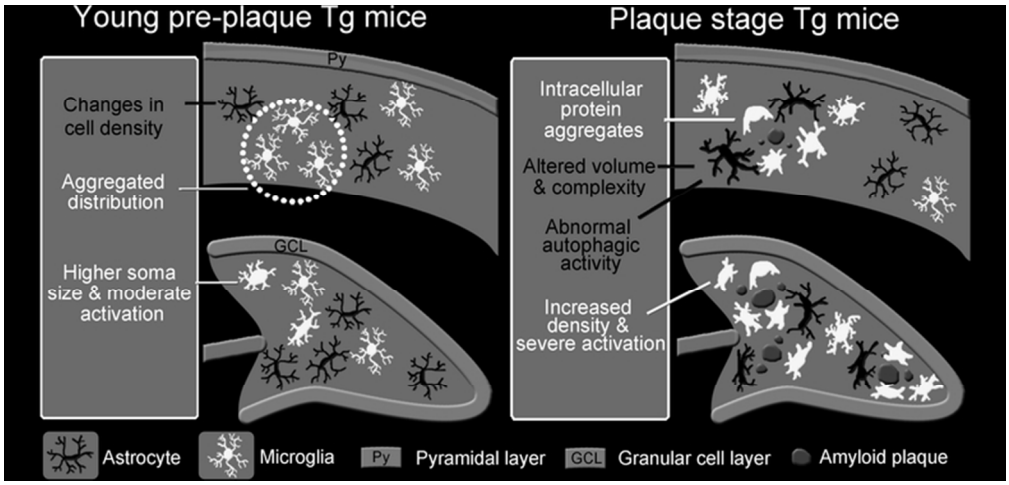

Figure 8/Graphical Abstract. Schematic representation of glial changes found in the hippocampus of PDAPP-J20 mice before and after plaque deposition. In each schema, a representative portion of two hippocampal subfields, the stratum radiatum (upper) and the hilus (bottom) is included. Several glial parameters are affected in the young pre-plaque mice. These changes were more pronounced and precocious in the hilus subfield. Amyloid deposition markedly aggravates the situation, promoting glia recruitment and increased reactivity. At advanced stages, astroglia increased LC3 labelling while microglia was strongly positive for ubiquitin and p62, suggesting altered autophagic activity.
66x31mm (300 x 300 DPI)

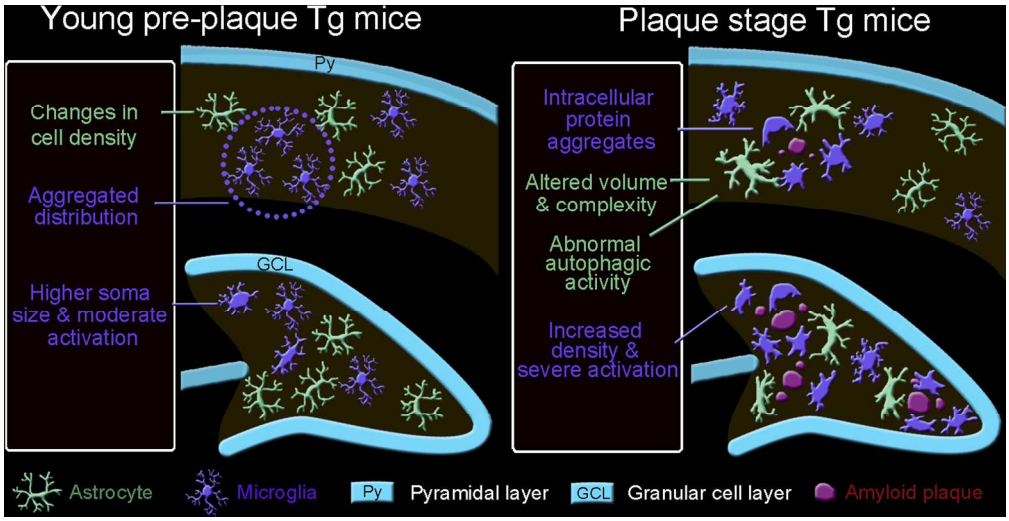

Figure 8/Graphical Abstract. Schematic representation of glial changes found in the hippocampus of PDAPP-J20 mice before and after plaque deposition. In each schema, a representative portion of two hippocampal subfields, the stratum radiatum (upper) and the hilus (bottom) is included. Several glial parameters are affected in the young pre-plaque mice. These changes were more pronounced and precocious in the hilus subfield. Amyloid deposition markedly aggravates the situation, promoting glia recruitment and increased reactivity. At advanced stages, astroglia increased LC3 labelling while microglia was strongly positive for ubiquitin and p62, suggesting altered autophagic activity.
129x66mm (300 x 300 DPI)

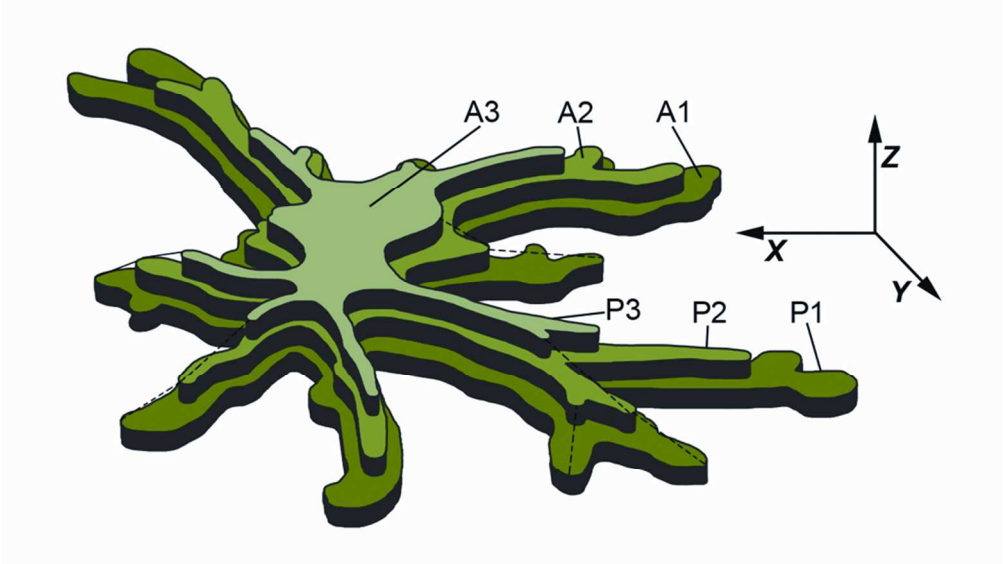

Supplementary Figure 1. Astrocyte Reconstruction.
Consecutive confocal images along the Z-axis were taken from coronal brain sections processed for GFAP immunofluorescence (tissue is on X-Y plane). In the figure, images from 3 different planes are represented. Complete and randomly selected astrocytes were considered for cell surface and volume estimation. GFAP+ area (A) and perimeter (P) were measured in each image with digital software. The single cell's volume was calculated assuming that the GFAP+ area does not change along the planes between consecutives images, as shown in the figure in dark-gray. On the other hand, the single cell's total surface was calculated considering that GFAP+ areas and perimeters change linearly in the space between consecutive images, as shown by dashed lines
90x50mm (300 x 300 DPI)